AN INVESTIGATION INTO THE BENDING OF POLYACENE STRANDS AND APPLICATIONS TO CARBON NANOTUBES AND TOROIDAL CARBON NANOTUBES:

A DENSITY FUNCTIONAL THEORY INVESTIGATION

by

Scott R. Buechler

A thesis submitted to the Faculty and the Board of Trustees of the Colorado School of Mines in partial fulfillment of the requirements for the degree of Master of Science (Engineering Systems – Mechanical Specialty).

Golden, Colorado

Date Jan 22, 2007

Signed: ______________________
Scott R. Buechler

Approved ______________________
Dr. Mark T. Lusk
Thesis Advisor

Golden, Colorado

Date Jan 22, 2007

____
Dr. Terry Parker
Director and Professor
Division of Engineering

ABSTRACT

Synthesized toroidal carbon nanotubes (TCNs) could offer significant applications in structural, magnetic, and electronic devices. Synthesis of these structures could be successful through the bending of long single-wall carbon nanotubes or undulating tubes of coalesced C_{60} molecules. For this method to be successful the mechanical properties of TCN structures must be well understood. A creation of this understanding motivates the present investigation.

This thesis investigation seeks to quantify the elastic properties of polyacene strands and rings in order to more completely understand the mechanical properties of TCNs and other fullerene structures.

Density functional theory calculations are used to determine the elastic responses to uni-axial tension and bending of polyacene strands. Additionally, a brief study of the curvature dependence of TCNs is conducted to offer insights into the bending modulus of single-wall carbon nanotubes. The result is a quantifiable description of the mechanical responses of simplified systems of polyacene strands and rings and their application to more complicated fullerene type structures.

TABLE OF CONTENTS

LIST OF FIGURES

LIST OF TABLES

ACKNOWLEDGEMENTS

I would like to take this opportunity to express my deepest gratitude to my advisor, Dr. Mark T. Lusk. His inspiration, knowledge, and guidance have been essential in developing me as a scientist and a person. Additionally, I would like to thank the members of my committee, my research group, and other professors at the Colorado School of Mines for aiding in my academic development. Finally, I would like thank my friends and family for the support and laughter they have given me over the past couple years.

CHAPTER 1

INTRODUCTION AND MOTIVATIONS

1.1 Mechanical Properties of Single-wall Carbon Nanotubes

Atoms are the foundation for the structure and elastic properties of any material, and the collective behavior of atoms dictates how materials deform. This has motivated the development of theoretical frameworks which link atomic scale phenomena to meso/macro properties [1]. For instance electronic structure and molecular dynamics analyses now routinely provide quantitative supplementary information to scientists pursuing materials development. This approach has been particularly successful in the recent wave of activity in nanotechnology driven by the novel electromechanical properties of fullerene structures.

In the past decade, carbon nanostructures have been studied intensely because of their potential engineering applications. The advantages of using carbon nanostructures include their electronic stability, biological compatibility, strength, flexibility, high thermal conductivity, and potential applications within the semiconductor industry. The beneficial properties of these fullerene structures can be integrated into a wide range of commercial and scientific applications including: composite materials, electronic applications and sensors, batteries, magnets, pollution elimination, insulation, actuators, and hydrogen storage [2] [3].

Numerous studies have been conducted on the elastic properties of carbon nanostructures [4] [5] [6] [7] [8] and the results for graphene and single-wall carbon nanotubes (SWCNTs) are summarized in Table 1.

	YOUNG'S MODULUS	POISSON'S RATIO
Graphite	1.06 TPa	0.19
SWCNT	0.40 to 4.15 TPa	0.16 - 0.20

Table 1. Summary of elastic properties of graphene and SWCNTs.

These studies have been conducted over a wide array of length scales, from the quantum mechanical to the meso-scale, thus providing a stable foundation for comparison. However, the range of data given prompts a desire for a concrete description of the elastic properties of these systems.

1.2 Torodial Carbon Nanotubes

Carbon nanotubes have received the most attention as elementary construction components, but other carbon fullerene structures may offer additional choices in materials design. Carbon nanotori, for instance, are extremely flexible and offer a high strength-to-density ratio [9]. Carbon nanotori, also known as toroidal carbon nanotubes (TCN) or simply nanorings, are simply single-wall carbon fullerene shells with the ends connected to create a torus. Since the idea of carbon nanorings was first introduced, there have been four TCN geometries theorized [10] [11] [12] [13] [14] [15]. The descriptions for the four TCN geometries and a summary of each can be found in [16]. Type I TCNs make use of pentagonal and heptagonal defects to induce curvature into a tube to form a completed torus [12] [13]. On the other hand, the beautifully symmetric Type II TCNs are toroidal polyhexes [14] created by joining the ends of a single-wall carbon nanotube

[15] [16]. Additionally, for sufficiently large radii tight-binding calculations show that Type II TCNs become energetically favorable over rings of pentagonal and heptagonal defects [15]. Potentially the most technologically promising and synthesizable are TCNs formed from C_{60} molecules connected through pentagonal and heptagonal rings [10] [11]. This construction forms an undulating tori referred to as a Type III TCN [16]. Finally, Haeckelite tubules [17] can be formed forming similar undulating rings to those in [10] [11]. Figure 1 is an isometric illustration of a Type II (5,5) TCN.

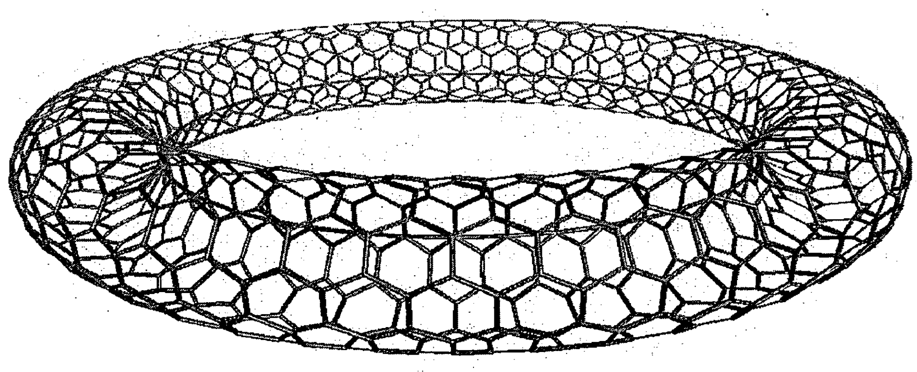

Figure 1. Perspective view of a Type II (5,5) TCN.

Interconnected nanorings offer design possibilities that exploit the properties of single TCNs in new ways. For instance, nanorings could be interconnected to form one-dimensional chains or a two-dimensional structure known as *nanomaile* [9]. Figure 2 shows an example of such a two-dimensional ring structure.

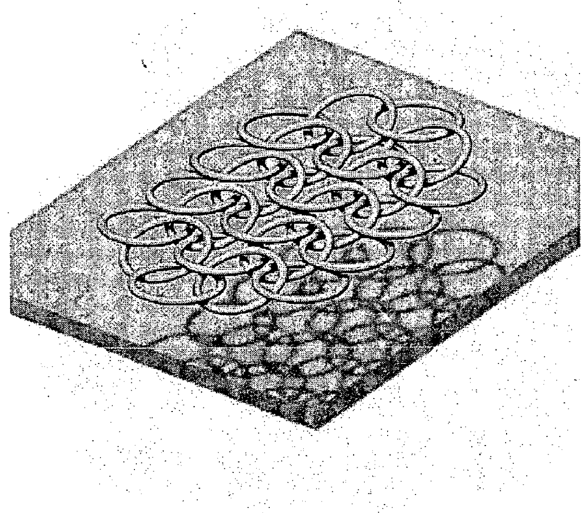

Figure 2. Two-dimensional carbon *nanomaile* structure [9].

One of the primary mechanical motivations for developing such complex carbon structures is their ability to handle extreme tensile stresses and strains, while maintaining complete reversibility. *Nanochains* and *nanomaile* can maintain completely reversible strains of 39% and 25%, respectively. In addition, these structures have tensile strengths in the range of 5.7 – 8.5 GPa and strength-to-density ratios that are approximately 15 – 20 times greater than steel and 1.5 – 4 times greater than spider silk [9].

Mechanical properties have not been the only focus for carbon nanostructures; others have focused on the electronic and magnetic benefits of these structures. Recently, the magnetic and conducting properties of carbon nanotori have become of increasing interest [10] [11]. One example is that of Liu's group from the University of Louisville. Liu's group has conducted theoretical experiments that demonstrate the novel magnetic properties of nanotori. In their analysis, a 0.1 Tesla magnetic field applied along the toroid axis is predicted to cause the spins of the electrons to line up producing a spin contribution to the magnetic moment. Additionally, though, they predict that special, conducting TCNs generate ring currents that result in a colossal paramagnetic moment. Liu and colleagues suggest that the characteristics of these nanotori arise from the unusual behavior of the electrons in the ring shaped structure [18] [19].

TCNs of Types I and II are only theoretical concepts and have not been synthesized but are believed to be mechanically stable [16]. Although there is no evidence of a formation mechanism for the toroid of polyhexes, a possibility is that a defect free SWCNT of sufficient length could be bent into a ring and the two ends connected. The energy required to bend a nanotube into a ring however would have to be less than the bond breaking energy. For this method to be successful the mechanical properties of the nanoring structure must be well understood; most importantly, the bending modulus. The creation of this understanding motivates the present investigation

Contrary to Types I and II, TCNs of Types III and IV have been realized experimentally through the coalescence of C_{60} molecules and have been proven to be demonstrably stable [10] [11][16]. This a significant achievement in nanotechnology since TCNs are no longer merely theoretical constructs. However their mechanical properties are yet to be fully understood. This lack of understanding further motivates an investigation to quantify the fundamental mechanical responses of graphitic and fullerene type structures. All toroidal structures have, to some extent, out-of-plane bending of graphitic sheets, and it is the resistance to such bending that is of particular interest in the current study. This bending property may be isolated by quantifying the mechanical response of polycyclic aromatic hydrocarbons to out-of plane bending. The results can then be generalized to carbon tubules and toroids.

1.3 Polyacenes and Polyacene Rings

Polycyclic aromatic hydrocarbons (PAH) are molecules consisting of fused aromatic rings with no heteroatoms. PAHs are formed from the incomplete combustion of carbon containing fuels. Of particular interest in this discussion are those that form in a linear "strand". This particular class of molecules are known as acenes or polyacenes. The simplest PA is the molecule naphthalene [20]. Its molecular structure is shown in Figure 3 with bond lengths and bond angles provided in Figure 4.

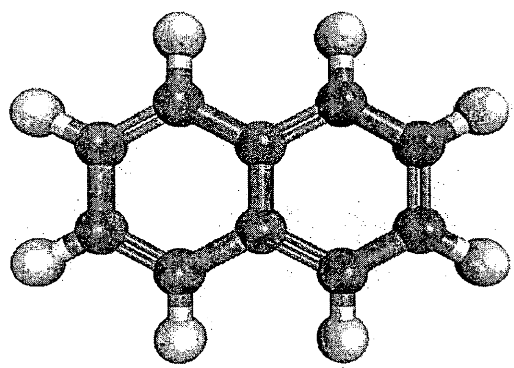

Figure 3. Atomic structure of naphthalene.

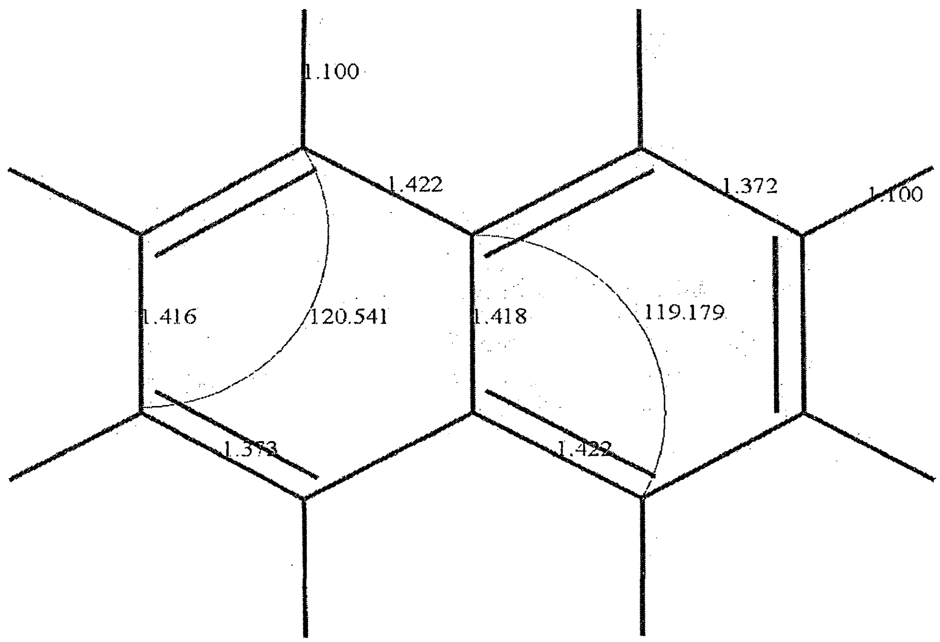

Figure 4. Lengths and bond angles for naphthalene.

The largest polyacene (PA) that has been synthesized is heptacene (7 aromatic rings) [20] but even that is known to be extremely reactive and unstable. Additionally, heptacene has not yet been isolated as a single strand; it has only been synthesized within a matrix. This molecule is of great interest to researchers due to its potentially beneficial electronic properties [20]. Many of the smaller PAs are known to be organic semiconductors.

As a theoretical construct, imagine a PA of reasonable length in which the ends are connected to form a ring. Such rings, termed PA rings in this thesis or cyclic polyacene [21], can offer valuable insights into the mechanics of carbon nanotori due to their graphitic like structures. In fact, they can be viewed as passivated slices of a carbon nanotube. Figure 5 shows time steps from a molecular dynamics simulation in which a theoretical force is applied to a PA with optimized ends to move selected atoms in a particular direction. The reduced scale and minimal complexity of the PA strands yields advantages in both computational efficiency as well as in the construction of a system in which parameters are reduced and localized effects can be fully understood. Using this system, mechanical properties can be decoupled from each other and from geometrically induced effects (i.e. curvature effects) and applied to understanding and designing more complicated carbon nanostructures.

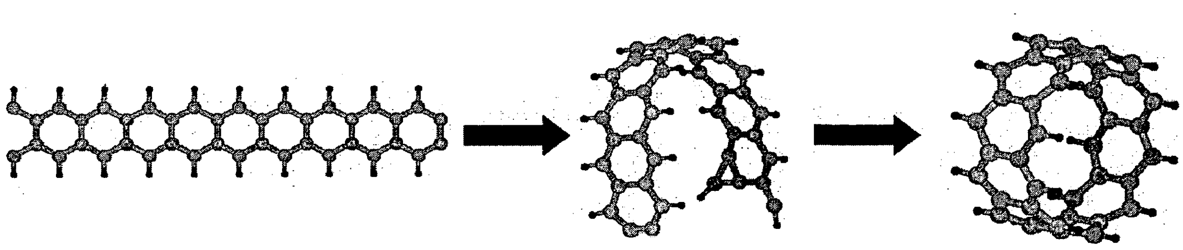

Figure 5. Illustrative model of the formation of a PA ring.

In this simulation the ends of the PA are simply moved toward each other to form a ring. The primary motivation for this model was a previous study into a formation mechanism for PA rings; however, it was determined that they could be used as clean systems to analyze pure bending of PA strands. No attempt in this thesis is made to quantitatively describe or propose a synthesis mechanism; it is simply intended to be an illustration of the process of forming a theoretical PA ring. The mechanics of PA ring models, can offer effective insights into the out-of-plane response of fullerene structures. For instance, such an analysis should enable the development of an estimate for the force/moment combination required to efficiently produce a Type II TCN using the same idea as is illustrated in Figure 5.

1.4 Scope and Objectives

This thesis investigation seeks to quantify the elastic properties of PA strands and rings in order to more completely understand the mechanical properties of TCNs. In Section 3.1.2, the Young's modulus of PA is evaluated and compared to published data for SWCNTs and graphene sheets. An in depth investigation is conducted in Section 3.1.3 of the complicated Poisson effect experienced by PA strands. Section 3.2 focuses on the bending response of PA strands with application to PA rings. The relation between bending properties and persistence length is considered in Section 3.2.2. Finally an analysis on the curvature effects of TCNs is provided in order to show how the PA strand behavior relates to the more complex setting of a fullerene torus of Type II.

This investigation utilizes density functional theory to quantify the elastic properties of simplified carbon nanosystems and to offer effective insights into the mechanics of carbon nanotori. As will be discussed in detail in Chapter 2, the real space density functional theory package, DMOL^3, was used as the primary analysis tool. Additionally, Chapter 2 discusses the motivation, advantage, and disadvantages of adopting a real-space DFT analysis strategy and the associated mechanics theory utilized in analyzing PA structures.

CHAPTER 2

Theoretical Approach and Computational Details

2.1 Density Functional Theory

Density Functional Theory (DFT) is a quantum mechanical analysis technique used in electronic structure calculations in both computational physics and chemistry. It is applicable to a broad range of molecular systems and can provide accurate calculations of structure, reaction energies and reaction barriers. Since the 1970s, DFT has been used extensively in chemistry and materials science because it produces reasonably accurate electronic structure calculations for a computational cost much less than other methods of analyzing many-body quantum mechanical problems. The physics community, especially those involved in solid-state physics, has come to accept and further develop DFT with a primary focus on K-space implementation. The prime objective of a DFT analysis is to solve a complicated many-body problem involving a large number of electrons by adopting the electron density, ρ, as the basic quantity to be solved for instead of the many-body wavefunction, $|\Psi>$.

DFT can be summarized by the following sequence:

$$\rho(\mathbf{r}) \rightarrow |\Psi\rangle \rightarrow V(\mathbf{r}) \tag{2.1}$$

in which V(**r**) is the external potential. This equation conveys the idea that knowledge of the density implies knowledge of the wavefunction and external potential. From the external potential (the potential energy acting upon the electrons) all other observables can be determined [22]. The DFT formalism is introduced here through an overview of its primary foundational concepts: electron density and its relation to basic quantum mechanical concepts; the variational principle and Rayleigh-Ritz method; Hohenberg-Kohn theory; Kohn-Sham theory; and, pseudopotentials.

2.1.1 Electron Density and Basic Quantum Mechanical Concepts

The time-independent wave function can be determined from the time independent form of Schrödinger's equation:

$$\left[-\frac{{h_{bar}}^2\nabla^2}{2m}+V(\mathbf{r})\right]\Psi(\mathbf{r})=\varepsilon\Psi(\mathbf{r})\,. \tag{2.2}$$

This calculation becomes intractable as the number of electrons increases beyond a small handful. However as will be discussed subsequently, this many-body problem can often be replaced by a much more manageable approximation involving the electron density, ρ.

$$\rho(\mathbf{r})=N\langle\Psi|\Psi\rangle \tag{2.3}$$

2.1.2 Variational Principle and the Rayleigh-Ritz Method

A fundamental concept in density functional theory (DFT) is the Variational Principle. In the overwhelming majority of systems there is no analytic solution to the time independent Schrödinger's equation (TISE). The lowest energy state of the system, E_o, and the corresponding ground state wavefunction, $|\Psi_o\rangle$, are often the quantities of interest.

The Variational Principle can be implemented to numerically approximate the ground state energy and associated wavefunction. Simply put, the Variational Principle is a statement that for any trial wavefunction, $|\Psi_{Trial}\rangle$, the expectation value of the Hamiltonian will be greater than or equal to the actual ground state.

$$E_o \leq \langle \Psi_{Trial} | H | \Psi_{Trial} \rangle \tag{2.4}$$

The trial wave function can be expanded as a linear combination of coefficients, c_i, and the eigenkets, $|\varphi_i\rangle$, of a simpler Hamiltonian. Orthogonality of these functions is guaranteed because of the Hermitian nature of all physically-based Hamiltonians.

The Rayleigh-Ritz method can now be applied to try and determine a set of coefficients, $\underline{c}$, to build an approximation for $|\Psi_o\rangle$ using a linear combination of eigenkets, $|\varphi_i\rangle$. An approach similar to this is also used in Kohn-Sham theory discussed later in this section. Begin, by defining a trial wave function such that

$$|\Psi_{Trial}\rangle = \sum_n c_n |\varphi_n\rangle . \tag{2.5}$$

Now a Rayleigh quotient can be defined as

$$\varepsilon = \frac{\langle \Psi_{trial} | H | \Psi_{trial} \rangle}{\langle \Psi_{trial} | \Psi_{trial} \rangle}. \tag{2.6}$$

Rearranging the expression leads to the form:

$$\varepsilon = \frac{\sum_i \sum_j c_i^* c_j \langle \varphi_i | H | \varphi_j \rangle}{\sum_i \sum_j c_i^* c_j \langle \varphi_i | \varphi_j \rangle}. \tag{2.7}$$

Two matrix operators, H and S, can now be defined as

$$\begin{aligned} H_{ij} &= \langle \varphi_i | H | \varphi_j \rangle \\ S_{ij} &= \langle \varphi_i | \varphi_j \rangle \end{aligned}. \tag{2.8}$$

The result is a simplified expression for ε.

$$\varepsilon = \frac{\underline{c}^*.[H]\underline{c}}{\underline{c}^*.[S]\underline{c}} \tag{2.9}$$

ε can now be minimized with respect to $\underline{c}$ to produce the following relation.

$$\frac{([H] - \varepsilon[S])\underline{c} + ([H] - \varepsilon[S])^T \underline{c}}{\underline{c}.[S]\underline{c}} = 0 \tag{2.10}$$

If $\underline{c}$ and Ψ_i are real values, then due to the fact that the [H] and [S] matrices are Hermitian

([H] = $[H]^T$ and [S] = $[S]^T$) results in a generalized eigenvalue problem represented in Equation 2.11.

$$[H]\underline{c} = \varepsilon[S]\underline{c} \tag{2.11}$$

It is apparent in Equation 2.12 that Equation 2.11 converts the system into a linear algebraic expression for unknown coefficients and this form is used in the self consistent approach in DFT.

$$\hat{H}|\Psi\rangle = E|\Psi\rangle \rightarrow [H]\underline{c} = \varepsilon[S]\underline{c} \tag{2.12}$$

E is now minimized to determine the ground state energy and the associated ground state wave function, $|\Psi\rangle$. As stated previously, the electron density, ρ(**r**), can be defined as

$$\rho(\mathbf{r}) = N\langle\Psi|\Psi\rangle. \tag{2.13}$$

in which N, is the total number of electrons. The Rayleigh-Ritz method outlined above is applied to the concepts introduced by DFT to fully characterize the ground state properties of a system.

2.1.3 Hohenberg-Kohn Theory

Modern DFT derives from the analysis of Hohenberg and Kohn which proved the idea that all ground state properties are functionals of the charge density, ρ [23]. Hohenberg-Kohn (HK) theory is captured in four theorems known as the HK theorems. The importance of the HK theory is emphasized in the First and Second HK theorems, giving rise to modern DFT techniques.

DFT states that the minimum of the energy function corresponds to a ground state of a many-electron system. This ground state energy is determined through the variational principle and can lead up to the wave functions, Ψ. The essence of HK theory is emphasized in the First HK theorem. The First HK theorem states that an external potential, $V(\mathbf{r})$, can be determined within a trivial additive constant by the density, $\rho(\mathbf{r})$ [24]. Proving this can be explained quite easily. Suppose there exists unique potentials, $V(\mathbf{r})$ and $V`(\mathbf{r})$ that differ by more than an additive constant, but have the same density. In other words each of these potentials will yield a respective Hamiltonian, $\hat{H}$ and $\hat{H}`$. Wave functions ($|\Psi>$, $|\Psi`>$), ground state energies ($E_o$, $E_o`$), and densities ($\rho = N <\Psi|\Psi>$, $\rho` = N <\Psi`|\Psi`>$) can now be determined from their respective Hamiltonians. Thus, it will be shown that $|\Psi> \neq |\Psi`>$. Application of $|\Psi>$ and $|\Psi`>$ to a Rayleigh quotient and for H shows

$$E_o < \left\langle \Psi` \middle| \hat{H} \middle| \Psi` \right\rangle = \left\langle \Psi` \middle| \hat{H}` \middle| \Psi` \right\rangle + \left\langle \Psi` \middle| \hat{H} - \hat{H}` \middle| \Psi` \right\rangle = E`_o + \int \rho(\mathbf{r})[v(\mathbf{r}) - v`(\mathbf{r})]d\mathbf{r} \quad (2.14)$$

and for H`:

$$E`_o < \left\langle \Psi \middle| \hat{H}` \middle| \Psi \right\rangle = \left\langle \Psi \middle| \hat{H} \middle| \Psi \right\rangle + \left\langle \Psi \middle| \hat{H}` - \hat{H} \middle| \Psi \right\rangle = E_o + \int \rho(\mathbf{r})[v`(\mathbf{r}) - v(\mathbf{r})]d\mathbf{r}\,. \quad (2.15)$$

Summing these results produces the following inequality

$$E_o + E`_o < E_o + E`_o \ . \tag{2.16}$$

From this inequality, it is apparent that V(**r**) and V`(**r**) cannot have the same ρ and thus ρ determines V. In other words, there is only one unique V for the ground state density. If V determines Ψ and all properties of the system, then ρ can be shown to determine Ψ and all properties of the system. More specifically, the ground state density determines all the ground state properties.

The Second HK theorem extends the usefulness of First HK theorem. A discussion of the Second HK theorem begins with a redefinition of the total energy.

$$E_v[\rho] = T[\rho] + V_{ee}[\rho] + \int \rho(\mathbf{r})v(\mathbf{r})d\mathbf{r} \tag{2.17}$$

T, V_{ee}, and $\int \rho(\mathbf{r})v(\mathbf{r})d\mathbf{r}$ represent the kinetic energy, electron-electron potential, and the external potential of the system, respectively. The subscript of the total energy, E, is used to emphasize that this energy is determined by V and a key point is to observe that they are all functionals of the density.

Applying the Variational Theorem it can be seen that for any positive trial density, $\tilde{\rho}$, that satisfies the condition $\int \tilde{\rho}(\mathbf{r})d\mathbf{r} = N$; the total energy at this trial density will be greater than or equal to the ground state energy.

$$E_v[\tilde{\rho}] \geq E_o \tag{2.18}$$

This can be proved easily by applying trial densities to a similar approach to that used in the First HK theorem. The ground state density can now be determined by minimizing $E_\upsilon[\rho]$ through a variational approach with respect to the density, subject to the constraint $\int \tilde{\rho}(\mathbf{r})d\mathbf{r} = N$.

In summary, HK theory provides two main principles essential to the development of DFT. First, HK theory states that no two external potentials that vary by more than an additive constant can have the same density. This implies that the density can be used to determine the external potential--i.e. the density corresponds to only one external potential. As discussed previously, the external potential can be used to determine $|\Psi\rangle$ and all other properties. As a result, the value for any expected ground state property can be ascertained from the ground state density. This is known as the First HK Theorem and is the heart of HK theory. Additionally, the Second HK theorem states that through the Variational Principle any non-trivial positive trial density which satisfies $\int \rho(\mathbf{r})d\mathbf{r} = N$ will yield an energy greater than or equal to the ground state energy, E_0. These two theorems lay the foundation for DFT and the Kohn-Sham (KS) approach to be discussed subsequently.

The HK theory does yield, in itself, a set of tractable differential equations. However, the all electron wavefunctions can be expressed as a linear combination of orbital functions. Kohn-Sham theory extends the HK formalism by applying this concept.

2.1.4 Kohn-Sham Equations

What is commonly viewed as the operational implementation of density functional theory formulation (DFT) was originally developed by Kohn and Sham. The Kohn-Sham [25] approach utilizes single-particle orbitals and electron densities. The problem then resembles a single-particle theory although many-body effects are accounted for through a generalized Hamiltonian which includes exchange and correlation contributions.

To begin, a more accurate definition of the total energy can be developed by understanding that the kinetic energy can be decomposed into a non-interacting kinetic energy (T_s) contribution and one describing the correlated portion (T_c). T_c will be included in the correlation term of the exchange correlation potential to be discussed subsequently. Equation 2.17 can be re-written as

$$E[\rho] = T_s[\rho] + U_H[\rho] + E_{xc}[\rho] + \int v(\mathbf{r})\rho(\mathbf{r})d\mathbf{r}\,. \qquad (2.19)$$

In this expression, T_s is the kinetic energy of the non-interacting particles of the system, U_H is the electrostatic potential, E_{xc} is the exchange-correlation energy, and the integral defines the external potential, V, which accounts for external influences such as a collection of nuclei.

Kohn-Sham theory is a reformulation of the HK formalism in terms of a trace of the density operator—the inner product of the eigenkets of the density operator. These eigenkets are referred to as the natural spin orbitals used in KS theory. Application of the Variational Principle to the KS definition of the total energy with respect to variations in $|\phi>$ leads to the following expression,

$$\left[-\frac{h_{bar}{}^2\nabla^2}{2m}+v_{eff}(\mathbf{r})\right]\phi_i=\varepsilon_i\phi_i \ , \tag{2.20}$$

in which v_{eff} is defined as

$$v_{eff}(\mathbf{r})=v(\mathbf{r})+v_H(\mathbf{r})+v_{xc}(\mathbf{r}) \ . \tag{2.21}$$

Here $v=\frac{\delta V}{\delta\rho}$, $v_H=\frac{\delta U_H}{\delta\rho}$, $v_{ex}=\frac{\delta E_{xc}}{\delta\rho}$. The density can now be expressed as

$$\rho(\mathbf{r})=\sum_i|\phi_i(\mathbf{r})|^2 \tag{2.22}$$

Equations 2.21 and 2.22 define what are known as the Kohn-Sham equations and replace the problem of minimizing E[ρ] (originally used to replace the many-body Schrödinger equation) with solving Equation 2.11 [22].

Before the details of applying the KS approach are discussed, a more detailed perspective will be provided for the potentials T_s, U_H, and V. Due to the decomposition of T into T_s and T_C, T_s is simply the kinetic energy of a system of non-interacting particles. Therefore, the total kinetic energy for a system of non-interacting particles, T_s, is simply the sum of the individual non-interacting particle's kinetic energy. In terms of orbitals, T_s holds the form

$$T_s[\rho]=-\frac{h_{bar}{}^2}{2m}\sum_i^N\int\phi_i^*(\mathbf{r})\nabla^2\phi_i(\mathbf{r})d^3\mathbf{r} \ . \tag{2.23}$$

The electrostatic potential, U_H, is just the Hartree energy discussed in the Thomas-Fermi approximation. A discussion of Thomas-Fermi theory can be seen in [22] and leads to an expression for U_H. U_H can be viewed simply as the electrostatic interaction energy of the charge density.

$$U_H[\rho] = \frac{q^2}{2} \int d^3\mathbf{r} \int \frac{\rho(\mathbf{r})\rho(\mathbf{r}')}{|\mathbf{r}-\mathbf{r}'|} d^3\mathbf{r}' \qquad (2.24)$$

The external potential, V, can be calculated through the following expression.

$$V[\rho] = \int v(\mathbf{r})\rho(\mathbf{r}) d\mathbf{r} \qquad (2.25)$$

E_{xc} is now the only unknown term that has not been given an explicit form. It is formally decomposed into $E_{xc} = E_x + E_c$. The exchange energy, E_x, is due to the Pauli principle, while E_c is due to correlations between electrons. The exchange energy can be written in terms of the orbitals,

$$E_x[\phi_i[\rho]] = -\frac{q^2}{2} \sum_{jk} \int d^3\mathbf{r} \int \frac{\phi_j^*(\mathbf{r})\phi_k^*(\mathbf{r}')\phi_j(\mathbf{r}')\phi_k(\mathbf{r})}{|\mathbf{r}-\mathbf{r}'|} d^3\mathbf{r}\,. \qquad (2.26)$$

However, there is no exact expression for this in terms of the electron density. The correlation energy, on the other hand, is the additional energy lowering obtained in a real system due to a mutual avoidance of electrons [22].

A good approximation for the exchange correlation energy is the local density approximation (LDA). The local density approximation is based on the known exchange correlation potential of the homogeneous electron gas as a function of density. For regions in which the charge density is slowly varying, the exchange correlation function is defined as

$$E_{xc} = \int \rho(\mathbf{r})\varepsilon_{xc}(\rho)d\rho \ . \tag{2.27}$$

LDA defines the exchange and correlation energies at any point in space as a function of the electron density at that point in space only and is the starting point for many density functional applications. Another exchange correlation function is the generalized gradient approximation, but that is not used in this investigation and will not be discussed.

Before discussing the self-consistent application of the KS approach, recall that the KS approach is an effective single body theory through the use of the natural spin orbitals. The natural spin orbitals can be approximated by a linear combination of atomic orbitals defined as

$$\phi_i = \sum_{\mu} C_{i\mu}\chi_{\mu} \ , \tag{2.28}$$

in which $C_{i\mu}$ are the orbital expansion coefficients and χ_{μ} are the atomic orbitals, or atomic basis functions. A crucial concept to keep in mind is that the natural spin orbitals, ϕ_i, are orthonormal functions. These basis functions are emplaced using several different methods listed here with an example DFT package: Gaussian functions [26] (Gaussian), Slater functions [27] (ADF), plane waves [28] (Castep), or numerical orbitals [29] ($DMOL^3$). From these definitions the system can now be solved by an iterative self consistent process.

The first step in the iterative process is to choose an initial set of expansion coefficients, $C_{i\mu}$. From the expansion coefficients, natural spin orbitals can be constructed using Equation 2.28. The density functional can now be determined as stated above, by summing over the square of the natural spin orbitals.

$$\rho(\mathbf{r}) = \sum_i |\phi_i(\mathbf{r})|^2 \tag{2.29}$$

Stemming from the fact that the atomic orbitals do not have to be orthonormal but the spin orbitals do, the Rayleigh-Ritz approach outlined in Section 2.1.2 recasts the system from Eq 2.20 into a linear algebra problem.

$$HC = \varepsilon SC \tag{2.30}$$

In which H and S are again defined as:

$$\begin{aligned} H_{ij} &= \left\langle \chi_i \middle| \left(-\frac{h_{bar}{}^2\nabla^2}{2m} + v_{eff}\right) \middle| \chi_j \right\rangle \\ S_{ij} &= \left\langle \chi_i \middle| \chi_j \right\rangle \end{aligned} \tag{2.31}$$

Expression of the density functional, ρ(**r**) as a linear combination of atomic orbitals allows H_{ij} and S_{ij} to be constructed explicitly and Equation 2.30 to be solved for the coefficients C. From this new natural spin orbitals, ϕ_i , and the density, ρ, can be determined. Now finally, if $\rho_{New} = \rho_{Old}$ the density has reached self consistency and the total energy can be calculated. If $\rho_{New} \neq \rho_{Old}$, then the process must be repeated until it is self consistent and $\rho_{New} = \rho_{Old}$.

2.1.5 Pseudopotentials

It is well known that most physical properties of solids are dependent on the valence electrons to a much greater degree than on the tightly bound core electrons [30]. The pseudopotential is an additional approximation on top of others used in the all electron calculations considered thus far (i.e. Born-Oppenheimer approximation, density functional approximations, and truncations of the wave function and orbitals) [31]. The primary goal of a pseudopotential is to approximate the complicated effects of the non-valence core electrons with an effective potential. The Perdew-Wang (PWC) [32] local correlation is an LDA pseudopotential fit to numerical results for a non-interacting electron gas. The PWC pseudopotential seperates out the correlation energies for high electron densities (small values of **r** -- core) and for low electron densities (large values of **r** – valence). Functional forms of these correlation energies can be seen in the PWC literature in [32]. Use of the LDA functional for studying graphitic and fullerene type structures has shown good agreement with experimental data [33].

2.1.6 Additional DFT Discussion

The purpose of this sub-section is to mention some application issues associated with DFT as well as to note the associated limitations. In DFT analysis, it is possible to perform both *spin-restricted* and *spin unrestricted* calculations. *Spin-unrestricted* refers to the use of different natural spin orbitals for different spin electrons, while spin restricted uses the same molecular orbital for spin-up electrons as it does for spin-down electrons. Throughout this thesis, spin-unrestricted calculations were conducted.

DFT is often considered an ab initio calculation; however, there are numerous approximations and empirical fits that are involved as much of this chapter indicates. In DFT, the theoretical formulation is exact but there are approximate expressions for the Hamiltonian and the total electron density. The LDA functional is a prime example of fitting empirical data into the DFT formalism. Despite improvement, DFT still has difficulty in describing intermolecular interactions--e.g. van der Waals forces, excited states, degenerate states, and weak interactions. Additionally, finite temperature effects are not accounted for in traditional DFT. Even though DFT is not truly ab initio it has been shown to be extremely accurate in a myriad of systems for a relatively low computational cost.

2.2 DMOL^3

DMol^3 is the predominant analysis tool used in this molecular mechanics study. It is a DFT package that employs a generalized linear combination of atomic orbitals (LCAO) approach. A very brief description of the advantages of DMol^3 is undertaken in this sub-section.

DMol^3 utilizes one of two functionals for DFT analyses based on the local density approximation: VWN [34] and PWC [32]. The PWC functional is used in this thesis. DMol^3 utilizes numerical orbitals, χ, as basis functions which are constructed from all electron calculations on isolated atoms. These basis functions amount to numerical values on an atomic-centered spherical polar mesh instead of analytic functions like Gaussian orbitals. An advantage of defining the orbitals this way is that, in a DFT context, the molecule can be dissociated into its constituent atoms and a reduction in the number of variables follows.

The nature of these atomic orbitals allows DMol^3 to use a fast convergent three-dimensional numerical integration technique to evaluate the hopping and overlap integrals associated with H and S equations, respectively. Specifically, the integrals for H and S are analyzed numerically using the following summations

$$\begin{aligned} H_{ij} &\cong \sum_i \chi_i(\mathbf{r}_i)\left(-\frac{h_{bar}{}^2\nabla^2}{2m} + v_{eff}\right)\chi_j(\mathbf{r}_j)\omega(\mathbf{r}_j) \\ S_{ij} &\cong \sum_i \chi_i(\mathbf{r}_i)\chi_j(\mathbf{r}_j)\omega(\mathbf{r}_j) \end{aligned} \quad (2.32)$$

The term $\omega(\mathbf{r})$ is simply a weighting function for each point in the spherical mesh used in the numerical integration.

Additionally, DMol^3 uses a *norm-conserving* pseudopotential. This implies that the all electron wavefunction and the pseudo wavefunction will produce the same charge density outside of the core radius. This is accomplished by requiring the integrals of the square of the amplitudes be the same; resulting in scattering properties represented correctly by the pseudopotential. Finally, DMol^3 incorporates an efficient approach for calculating the electrostatic potential to increase its efficiency and accuracy. The development and details of all of these DMol^3 properties can be found in the DMol^3 user's manual and [35].

Throughout this investigation, geometry optimizations are conducted under spin unrestricted conditions using the PWC-LDA functional and employing symmetry options to maximize efficiency. Moreover, the finest convergence criteria are applied resulting in an energy convergence within 1.0×10^{-5} Ha. DMol^3 is validated in Section 2.5.2 by determining the mechanical properties of a SWCNT with a comparison to published results.

2.3 SIESTA

A second DFT package was also used in this thesis research: Siesta (Spanish Initiative for Electronic Simulations with Thousands of Atoms). This is a density functional method for electronic structure calculations and ab initio molecular dynamics. The primary niche of this DFT software is its applicability to very large systems with relatively low computational demands. As with $DMol^3$, Siesta uses standard pseudopotential forms and numerical LCAO for the basis set. The LCAO are nonorthogonal bases, and like $DMOL^3$, reduce the number of variables substantially compared to plane wave and other real space methods. Additionally, the basis functions and the electron density scale linearly with the size of the system. Siesta was used in this research project as an analysis technique to provide additional checks on the results of $DMOL^3$ for the mechanics of PA systems. Documentation detailing Siesta can be found in references [36] and [37]. Furthermore, a user guide detailing the applications and parameters can be found at:
http://www.uam.es/departamentos/ciencias/fismateriac/siesta/

2.4 ReaxFF

Beginning in the 1970s, computational performance enabled molecular dynamics (MD) to become a primary tool for molecular investigations in materials science, physics, and chemistry. The focus of MD is typically on length and time scales larger than those associated with DFT, and the approach allows finite temperature studies to be performed.

As with DFT, though, MD is a computational tool for elucidating the behavior of molecular systems. It is used in a wide array of scientific fields to investigate topics from biophysical research of protein folding to materials science developments of thin film deposition. More recently, MD has been used in examining the physical properties of nano-devices that often times have not even been created yet.

Traditionally, MD codes are extremely valuable tools in molecular modeling, but the force fields used are unable to model chemical reactions because of the requirement of breaking and forming bonds [38]. ReaxFF, however, is a force field for reactive systems to study molecular dynamics of large scale chemically reactive systems. ReaxFF uses a general relationship between bond distance and bond order and between bond order and bond energy that leads to proper dissociation of bonds to separated atoms. Additionally, other valence terms are present in the force field (angle and torsion). These terms are defined in terms of the same bond orders so that all of these terms go to zero smoothly as bonds break [38]. Finally, ReaxFF includes Coulomb and Morse (van der Waals) potentials to include the interactions between non-bonded atoms.

This investigation utilizes ReaxFF for a general comparison of mechanical properties of PA strands and rings. As a point of reference, all ReaxFF simulations conducted in this study are conducted at low temperatures (less than 30K) and use a 0.25fs time step. It has been shown that ReaxFF is accurate and efficient in calculating typical hydrocarbon properties [38] and is used in this investigation to effectively determine mechanical properties of PA systems.

2.5 Mechanics Approach for Graphitic and Fullerene Structures

This investigation will focus on three primary structures: PA strands, graphene sheets, and SWCNTs. These structures will provide the foundations for investigating the mechanics of fullerene systems.

2.5.1 Geometrical Properties of Graphene and SWCNTs

PA strands were introduced previously; therefore, the purpose of this sub-section is give parity to the other fullerene structures, by explaining their structure and geometric properties.

Graphene is a single planar sheet of graphite and solely comprised of sp^2-bonded carbon atoms. Pure graphene is constructed of aromatic hexagonal carbon cells with no pentagonal or heptagonal cells. Pentagonal and heptagonal members are considered defects and will induce curvature into the system. A carbon nanotube can be geometrically constructed by simply rolling a graphene sheet. However, the nature of the rolling --i.e. the chirality--defines interesting electronic and structural properties.

The chiral vector, $\mathbf{C_h}$, defines a vector which connects two crystallographically equivalent sites of a two-dimensional graphene sheet. This chiral vector is defined as:

$$\mathbf{C}_\mathbf{h} = n\mathbf{a}_1 + m\mathbf{a}_2 \equiv (n, m) \tag{2.33}$$

$\mathbf{a_1}$ and $\mathbf{a_2}$ define the graphene lattice vectors, while n and m are simply integer magnitudes [39]. A graphical representation of this is in Figure 6.

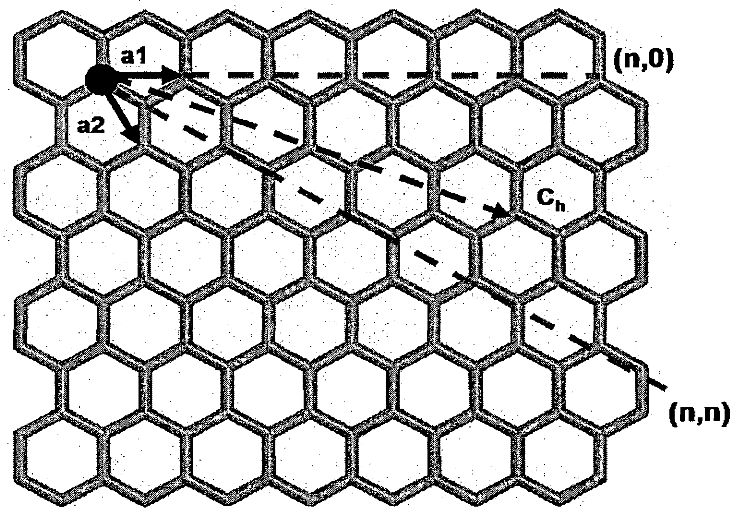

Figure 6. Geometric definition of the chiral vector, C_h, for SWCNTs.

The chiral vector determines whether a SWCNT behaves metallically or as a semiconductor. Zigzag nanotubes are defined SWCNTs with chiral indices of the form (n,0). Such nanotubes will be metallic for n/3 and semiconducting otherwise. When the chiral angle rotates 30° from (n,0), n will equal m and this is known as an armchair configuration [39]. SWCNTs of this configuration will be metallic for all values of n. More generally, tubes can have any integer-valued indices (n, m). These are referred to as chiral nanotubes. A more in depth discussion of these properties can be found in [39].

2.5.2 Young's Modulus

Strain energies, molecular geometry, and elastic shell theory are utilized to calculate mechanical properties--i.e. Young's modulus, Poisson's ratio, and the bending modulus--of SWCNTs and PA strands. In studying the mechanical properties of graphitic and fullerene type systems, the following simple system will be used as a demonstration and validation of defined methods. Visualize the (5,5) SWCNT and accompanying periodic unit cell of Figure 7.

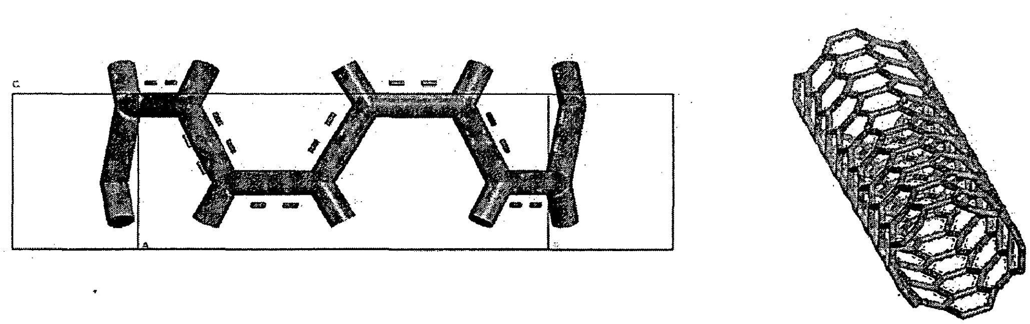

Figure 7. Periodic (5,5) SWCNT unit cell and super cell isometric view.

From this initial condition, an initial geometry optimization using a density functional theory code can be implemented to determine the initial equilibrium electronic structure. Following this, the periodic cell could be stretched in the axial direction, thus inducing an applied strain. The total energy in the system can now be determined for the corresponding applied strain. The initial condition forms a lowest energy state, or *base energy*. The energy change between the strained cases and the base case yields the strain energy. A parabola can then be fitted to the data to determine a function for strain energy as a function of the applied strain. A (5,5) SWCNT nanotube investigation was conducted in DMol^3 with a convergence criteria of 1.0e-5 Ha and a k-point sampling of 1x1x10 (in which 10 k-points are used in the periodic direction). This investigation results in the data presented in Figure 8 for strain energy as a function of strain.

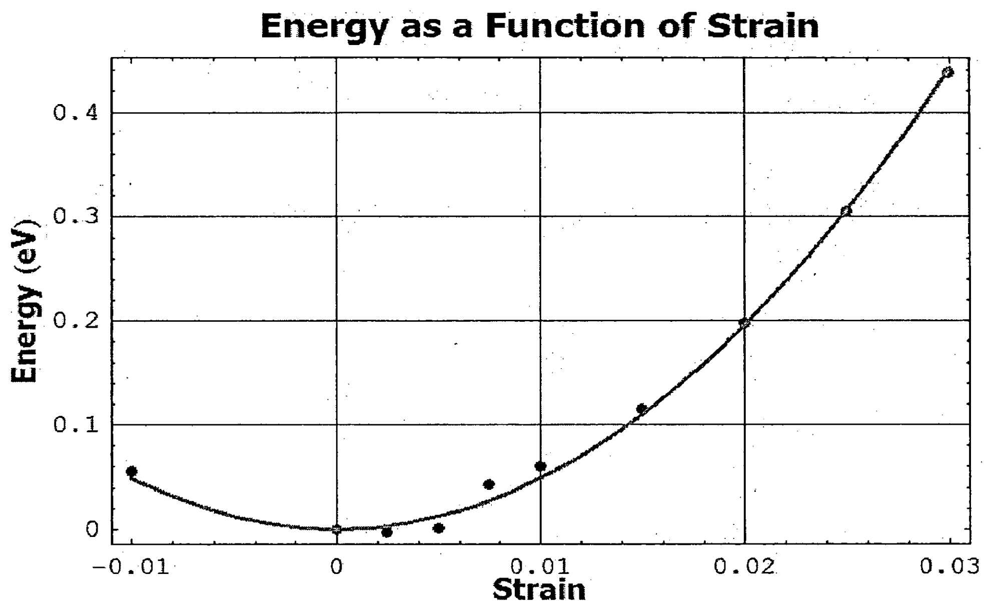

Figure 8. Energy as a function of periodic unit cell length (5,5) SWCNT.

As shown, strain energy calculations usually fit well to a parabolic fit, with the fit having the following form:

$$U_{Strain} = 489.954x^2. \tag{2.34}$$

The fitting function can now be transformed into terms of the change in length and the derivative of this function will then produce the applied force as a function of length.

This function for force can now be transformed back into a function of strain. From the force function, the stress in the system can easily be determined using the standard definition:

$$\sigma = \frac{F}{A} \, . \tag{2.35}$$

Here, A is the cross-sectional area of the system and F is the applied force. There are many opinions about the appropriate way of measuring the area, A, but the method implemented in this investigation is as follows. When looking at the graphitic structures investigated in these systems the cross-sectional area is determined using the distance between non-interacting sheets of graphite. In other words, if we were modeling a single sheet of graphite, graphene, the height component of cross-sectional area would be half the distance between non-interacting sheets of graphite on either side of the graphene. The width would be defined using a similar approach in which the width would be determined by the width of the molecule plus half the distance of a C – C bond on either side. Figure 9 depicts the height component graphically.

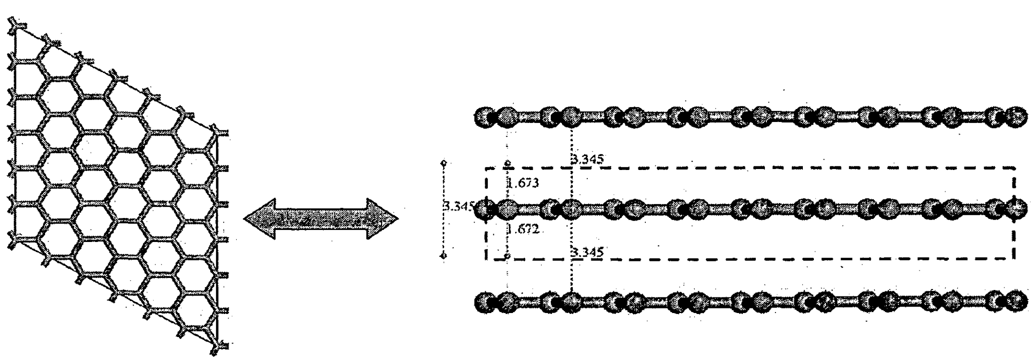

Figure 9. Graphical concept of cross-sectional area for graphene.

Calculation of cross-sectional area for nanotubes is accomplished by applying the separation distance between non-interacting graphene sheets in the previous discussion to the radius of the single-walled nanotubes. Figure 10 depicts an exaggerated form of this.

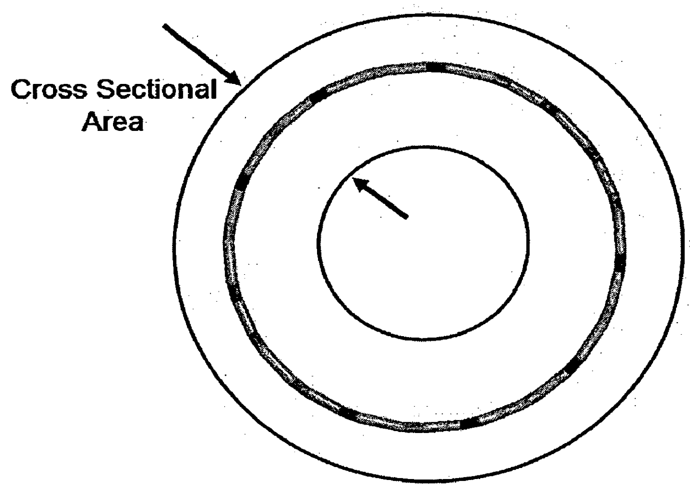

Figure 10. Exaggerated view to illustrate the calculation of the cross-sectional area of a SWCNT.

The cross-sectional area descriptions discussed form an elastic shell. This elastic shell model has been applied within the field [9] [40] and, as will be discussed subsequently, agrees well with experimental and modeling results. From this good agreement with experimental results, it can be assumed that the cross-sectional areas do not change substantially with relatively small applied loads. Application of the cross-sectional area measurement allows stress-strain data to be produced. An example of such data is provided in Figure 11.

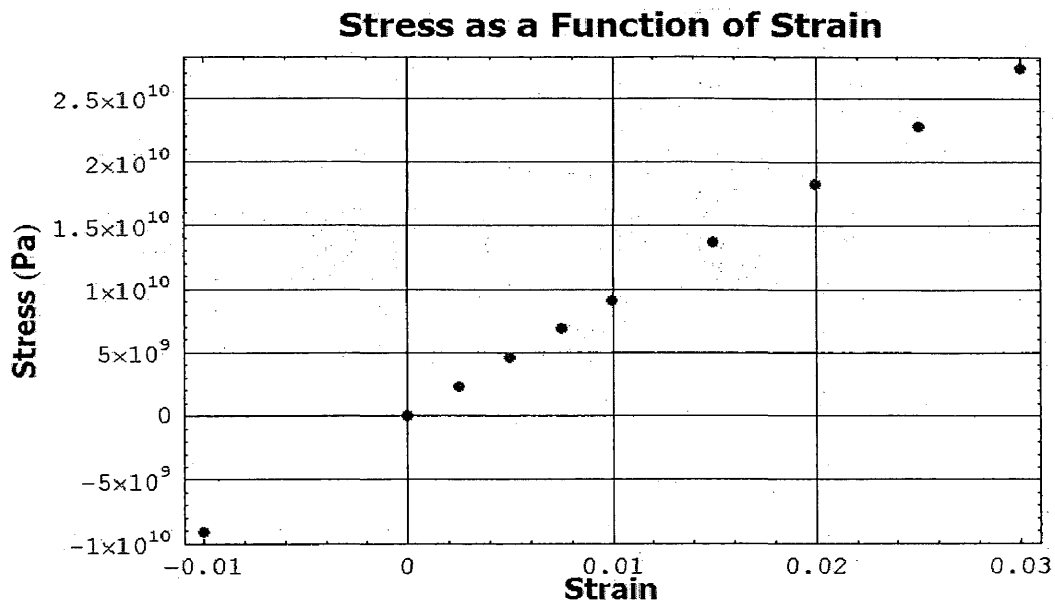

Figure 11. Stress as a function of strain for a (5,5) SWCNT.

Application of Hooke's Law

$$\sigma = E * \varepsilon, \tag{2.36}$$

then allows the Young's Modulus, E, to be determined.

DFT calculations using DMol^3 produce a value of E = 0.912 TPa for the Young's Modulus of a SWCNT. There have been many theoretical and experimental studies of SWCNTs reporting values ranging from 0.40 to 4.15 TPa [5]. The calculated value of E = 0.912 TPa fits within this range. Additionally, researchers using a LDA density functional code applying the concept of linear combinations of atomic orbitals reported values $E \approx 0.80 - 1.00$ TPa for multi-walled nanotubes and single-walled nanorope. The researchers conducting this study are some of the authors of the DFT package Siesta described above. Running a (5,5) SWCNT simulation similar to the one conducted using DMol^3 in Siesta yields E = 1.085 TPa.

More importantly experimental studies for graphite [8] have yielded a result of E = 1.06 TPa. Applying similar methods to those discussed for SWCNT, it was seen that DMol^3 produced a Young's modulus for graphene of E =1.059 TPa. This shows a very strong agreement between modeling and experiments for both graphene and SWCNTs supporting the theoretical development discussed here. From these comparisons it can be concluded that DMol^3 reports electronic structure of carbon systems accurately.

From the close comparisons between the molecular structure of graphene and a PA strand, the difference between experimental and DFT calculated Young's moduli for graphene will be used to quantify the error in the DFT calculations. An investigation comparing the cohesive energies calculated using the LDA-PWC functional for a number of different systems was done with a comparison to experimental values. In comparing the cohesive energies for carbon systems, graphite, diamond, and a C_{60} molecule were calculated. It was found that the differences between the cohesive energies in LDA and experiment for graphite, diamond, and a C_{60} molecule were 1.57, 1.63, and 1.22 eV/atom respectively. These values show a large departure from experiment, but it has been observed that LDA generally overestimates cohesive energies. Furthermore, simulations were conducted for Si and Ge due to the nature of the valence electrons with respect to carbon. In these systems it was seen that LDA differed from experiment by 0.71 and 0.88 eV/atom respectively. From these values no clear quantifiable error can be determined, because there is a large deviation in the overestimation of the cohesive energies.

More specifically, in this investigation the differences in energy are of concern, not necessarily the magnitudes. Therefore, using the Young's modulus of graphene for a quantifiable error is the most appropriate choice because it is a comparison for a differential energy measurement of a similar molecular structure. Therefore, even though it is seen that LDA does not calculate the magnitudes of the cohesive energies with a great deal of accuracy it can be seen that the change in energies is reported accurately. Comparing the Young's modulus for graphene using LDA and experiment shows a difference of 0.094%. Applying this to strain energy yields a range of error on the order of 0.0001 eV. Due to the fact that the range of strain energies calculated is on the order of 1 eV these error bars will be excluded from the subsequent plots.

2.5.3 Poisson's Ratio

A material that is loaded in one direction will experience strains perpendicular to that of the loading direction. This ratio of the transverse strain (perpendicular to the loading direction) and axial strain (parallel to the loading direction) is known as Poisson's ratio, υ, defined in Equation 2.37.

$$\nu = -\frac{\varepsilon_{Transverse}}{\varepsilon_{Axial}} \tag{2.37}$$

This calculation is easily made by investigating the geometries of the relaxed strained structures. In both systems, PA strands and single-wall carbon nanotubes, the structures are fixed in the direction of loading, but are allowed to relax in the perpendicular plane, thus experiencing Poisson effects. As a result of in-depth PA strand investigations, it has been seen that depending on bond orientation, different bonds experience different effects. It can be shown that these non-uniform effects can be combined to describe bulk properties. The complexities of these effects will be discussed in much greater detail in accompanying sections.

2.5.4 Bending Tests

In isotropic materials, mechanical response is completely determined by two elastic constants—e.g. Young's modulus and the bulk modulus. The bulk modulus can also be determined using Young's modulus and Poisson's ratio. Unfortunately, the structures analyzed in this system are not isotropic. A primary motivation for investigating bending in these systems is to examine the potential in developing carbon nanotori. PA strands offer a simplified system in which specific parameters can be fully developed. By conducting theoretical bending tests on PA strands the bending modulus can be determined.

A general method in determining the bending modulus of a material in standard continuum engineering problems is the case of pure bending. The simplest case of pure bending is a beam possessing a vertical axis of symmetry subject to equal and opposite end moments. A geometric representation of this case is seen in Figure 12.

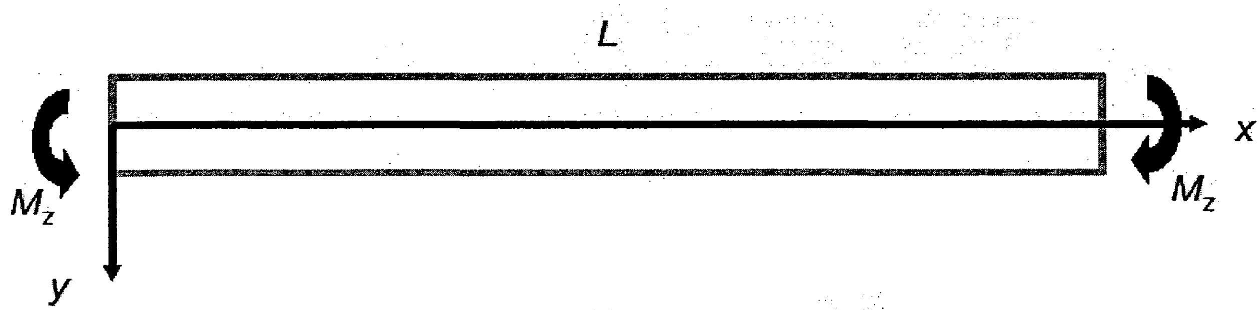

Figure 12. Pure bending model.

The pure bending model can be extended to a system in which the length of the beam is equal to a circumference of $2\pi r$. Thus, the beam would wrap around to form a complete circle, or "ring" in our case. In the system of a ring, the effects on the strain energy are localized completely to the curvature of the ring. If the energies between rings of different curvatures are measured, then the functional effect of the curvature on the strain energy can be determined. A schematic of the geometry is shown as Figure 13.

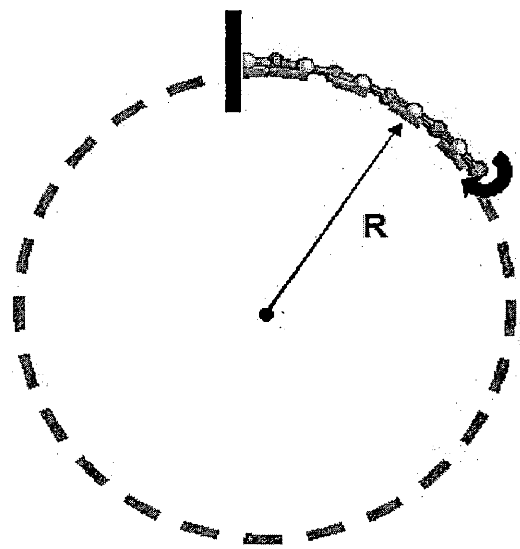

Figure 13. PA ring schematic.

Now that the geometric parameters have been introduced, the mechanical theory for this study can be discussed. The strain energy is defined as the difference in the energies between a PA ring of curvature, κ, and a PA strand of equal length with no curvature. Applying the expression $\sigma = -\frac{My}{I}$ for the stress, σ, the strain energy for a bending load is defined as

$$U = \int_V \frac{\sigma^2}{2E} dV = \int_V \frac{(-My/I)^2}{2E} dV = \int_0^L \frac{M^2}{2EI^2} (\int_A y^2 dA) dx \ , \tag{2.38}$$

in which M is defined as the bending moment, I is the second moment of area, and E is a bending modulus parameter. Again, the elastic shell assumption is made in determining the geometric properties that define I. As stated previously, the method of determining these geometric properties is validated for both experiments and modeling in Section 2.5.2. Recognizing the fact that $\int_A y^2 dA) = I$, and integrating with respect to x yields the following expression for the strain energy:

$$U = \frac{M^2 L}{2EI} \tag{2.39}$$

From mechanical analyses of pure bending it is well known that

$$\frac{M}{EI} = \frac{1}{R} = \kappa \quad , \tag{2.40}$$

in which R is the radius of the beam in bending. Substitution of this definition produces the following relation for the strain energy.

$$U = \frac{EI}{2} \kappa^2 L \ . \tag{2.41}$$

Equation 2.41 gives a simply expression for the strain energy of PA strands in bending as a function of curvature. In the case of a PA ring there is a boundary condition that is imposed. This boundary condition is that the length of the "beam", is equal to the circumference of the ring—$L = 2\pi R$. Applying the circumferential definition for L yields a more specialized form.

$$U = \pi E I \kappa \tag{2.42}$$

Equation 2.4.2 will be used in comparison to the DFT data obtained in Section 3.2.

CHAPTER 3

RESULTS

3.1 Axial Loading of Polyacene Strands

Axial loading is a predominant tool applied in the mechanics field to determine the Young's modulus of materials. It will be applied here to determine the Young's Modulus of PA strands.

3.1.1 Initial Geometry and Simulation Parameters

Figure 3 in Section 1.3 illustrates the shortest PA, naphthalene. To eliminate the addition of length dependent energetic and structural effects, a periodic unit cell is considered in the PA mechanical analysis which implies an infinitely long PA strand. In addition, a periodic unit cell with only 12 atoms maximizes computational efficiency. As a point of reference for larger clusters, surface effects become negligible as the system approaches that of a periodic unit cell. 12 atoms were chosen instead of the 6-atom minimum unit cell to ensure the complete aromatic effects of a complete hexagon would be captured inside the periodic cell. Removing finite length effects isolates the molecule from external parameters to provide a system in which the axial effects can be uniquely characterized. Figure 14 shows the periodic atomic structure at the zero strain condition in units of Angstroms (Å) and the direction of the applied loading:

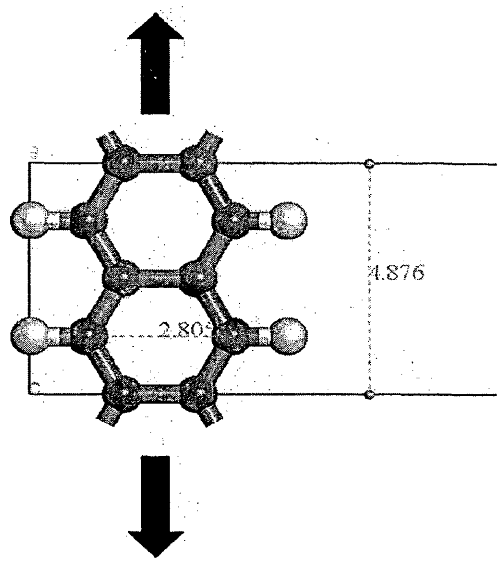

Figure 14. Polyacene strand periodic unit cell at the zero strain condition.

As a point of reference, DMol^3 expands out the period unit cell to a length in which finite length effects are not experienced; therefore, this initial configuration is not truly infinitely periodic. The theoretical development and definition of parameters for the DFT calculations performed in this investigation using DMol^3 were discussed in Section 2.1 and 2.2. These parameter settings, applied to a uni-axial tension experiment of the PA cell result in a k-point sampling of 1x5x1.

3.1.2 Young's Modulus

The periodic unit cell causes the axial length of the PA strand to be fixed consequently "constraining" the atoms along the loading axis but allowing them to relax with respect to the transverse axes. The fixed strain induces a strain energy, which can be used to determine the axial stress in the system. The assumption of a parabolic relation between strain energy and strain (Hooke's Law) allows the constant of proportionality (Young's Modulus) to be estimated.

The structures of benzene and graphene are used to estimate the zero-strain atomic structure for the PA strand. Unfortunately, the geometric structures of these two structures are not exactly that of PAs. Graphene does not have finite width effects, while benzene is completely passivated by hydrogen. Therefore, the zero-temperature equilibrium structure of these two systems was used only as a starting point in determining the zero-strain initial PA strand structure. A simulation was run in CASTEP utilizing the cell optimization routine in order to determine the relaxed equilibrium structure. The analysis allowed the dimensions of the unit cell to be optimized in addition to the optimization of the electronic structure thus allowing the system to reach an equilibrated periodic structure. This forms the initial structure on top of which axial strains are applied. DFT simulations for various axial strains yielded data for the total energy in the system as a function of the applied strain. Figure 15 shows a plot of the strain energy/strain data and the parabolic fit to this data.

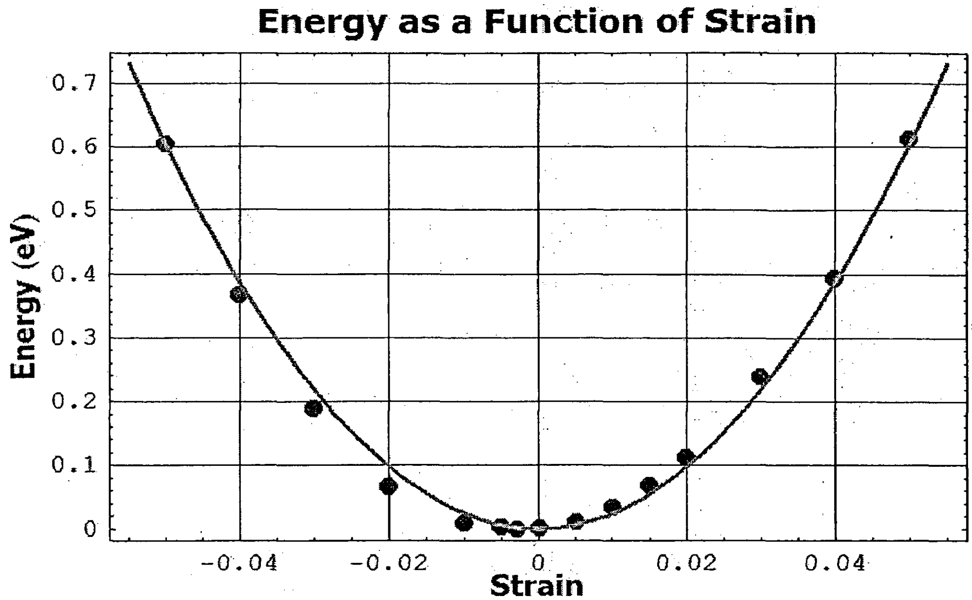

Figure 15. Energy vs. strain for axial loading of polyacene strands.

From Figure 15 it can be seen that the predicted zero strain geometry is in fact not the lowest energy state and thus not the actual zero strain atomic structure. Additionally, it can be seen that this data is not harmonic (in other words the energy changes due to small positive/negative strains is not the same). Due to the flexibility of the simulations to relax in the transverse directions we can translate the strain values of our data to represent correct applied strains. A simple minimization of the fitting function determines the strain value corresponding to the lowest energy state. This value was subsequently adopted to represent the zero strain or reference condition. The minimum energy occurs at a strain of -0.28%. Consequently, the strain data is translated in the positive direction by 0.28%. In later discussions the translated applied strain is transformed into the change in periodic unit cell length, ΔL, using the basic definition of strain:

$$\varepsilon = \frac{\Delta L}{L_o}. \tag{3.1}$$

Here L_o = 4.875703 Å is taken as the reference length at the translated zero strain point. Additionally, at the zero strain condition the minimum energy is approximately $U_{zero\text{-}strain}$ = -8288.45 eV. From this, the strain energy can be calculated using the simple relation—as was done above:

$$U_{Strain} = U(\varepsilon) - U_{zero-strain}. \tag{3.2}$$

Figure 16 shows a plot of the strain energy and translated strain values and its corresponding parabolic fitting function.

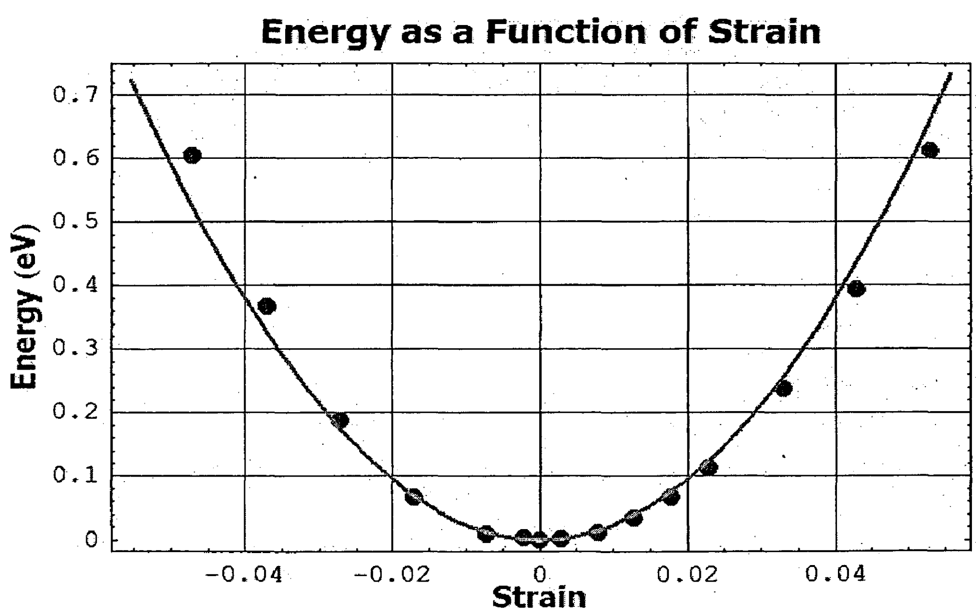

Figure 16. Strain energy vs. periodic cell length for polyacene strands in axial loading.

As can been seen in Figure 16, a parabolic fit fits the data extremely well and is expressed in Equation 3.3. An important observation is the harmonic nature of this fit.

$$U_{Strain} = 236.4x^2 . \tag{3.3}$$

Following the mechanics approach discussed in Section 2.5.2, this function can be translated into terms of the change in length and the derivative of the strain energy yields a linear relationship for the force. Conversion back from the change in periodic unit cell length to strain yields a linear relationship for the force as a function of strain. From this force, the stress experienced by the molecule is easily determined using the cross-sectional area. As mentioned previously, the method of determining the cross-sectional area of the system is paramount. Figure 17 depicts the cross-sectional area for PA strands following the procedure outlined in Section 2.5.2. In Figure 17 A = 3.354 Å, while B = 4.0476 Å. As in the case of graphene, A is simply the separation distance between non-interacting graphene sheets centered about the PA structure. The distance $A/2$ is the distance that the effect of one graphene sheet no longer has a substantial effect on another sheet. B is defined using the same concept, but is the width of the PA strand plus half the distance of a C – C bond on either side. This is an assumption made here, but forms a basis in defining the geometric description of a PA strand.

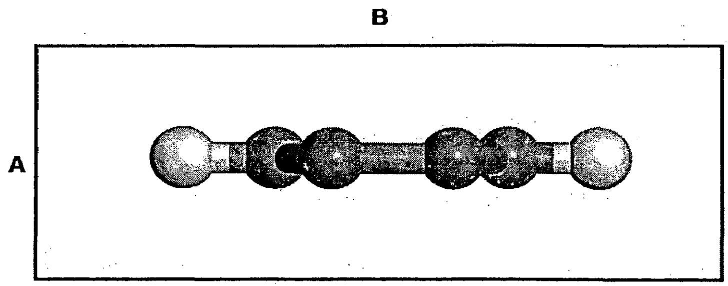

Figure 17. Cross sectional area of a polyacene strand.

The adopted definition of cross-sectional area definition yields stress/strain data illustrated in Figure 18.

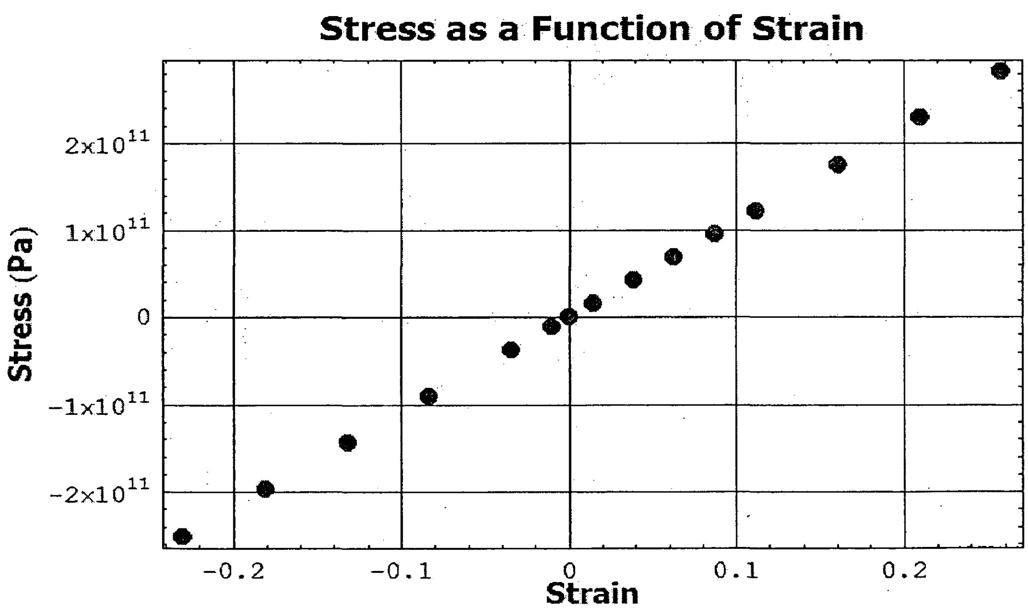

Figure 18. Stress vs. strain for axial loading of polyacene strands.

As expected, there is a simple linear relationship in which the slope can be calculated to determine the Young's Modulus of the system. The proceeding real-space DFT simulation using $DMOL^3$ and a 12-atom periodic cell results in a Young's Modulus of E = 1.093 TPa. In Section 2.5.2, the Young's Modulus was calculated in a similar fashion for a SWCNT, with a predicted value of E = 0.912 TPa. As with the SWCNT the PA strands should and do have essentially the same Young's Modulus as graphite. The accepted value for graphite is 1.06 TPa [8]. Although it is disputed whether the rolling of a graphene sheet affects the Young's Modulus of a SWCNT there are many theoretical and experimental studies of SWCNTs values for elastic constants ranging from 0.40 to 4.15 TPa [5]. This was discussed in detail in Section 2.5.2. Intuitively, a nanotube with armchair chirality, graphene, and PA strand should exhibit similar responses to uni-axial tension. The experimental and modeling agreement of these three structures implies that the assumptions made in defining the geometric properties are correct.

The DFT results using $DMOL^3$ were supported by calculations using Siesta and ReaxFF. Calculations performed in ReaxFF were conducted on a 39.18994 Å strand of PA at a temperature of 5 K. It was determined that finite length effects were negligible with respect to the periodic unit cell geometry for this length of PA strand. The Young's modulus values for the three different packages are summarized in Table 2.

	DMOL3 (DFT)	**SIESTA (DFT)**	**REAXFF (MD)**
Young's Modulus, E	1.093 TPa	1.091 TPa	1.360 TPa

Table 2. Young's modulus for a polyacene strand using three different analysis tools.

As indicated by the values in Table 2 there is good agreement between the two real-space DFT codes. The molecular dynamics value does differ from DFT results, but is still within a reasonable degree of error and well within the range of published values.

3.1.3 Poisson Effect

Further analysis of the electronic structure calculations of the axial loading of PA strands illustrates the effects on the transverse strains. If the transverse strains can be effectively measured, a Poisson ratio can be calculated via the method discussed in Section 2.5.3.

An initial investigation of the lateral strain for each axial strain case yielded a Poisson ratio of $\nu \approx 0.32$. This result is much larger than published Poisson ratios for sheets of graphite and SWCNTs: $\nu \approx 0.19$ for graphite $\nu \approx 0.16 - 0.20$ in SWCNTs [6][8][41][42]. The error in the initial investigation was eventually attributed to the fact that the Poisson effect was only analyzed at one point in the system--i.e. only one localized width measurement. Upon completion of a more detailed investigation of the optimized atomic structure of the strained PA systems, it was found that the angled C – C bonds experience a different Poisson effect then the horizontal C – C bonds. Figure 19 illustrates a distorted version of this effect and the two width measurements: $w_{+Poisson}$ and $w_{-Poisson}$:

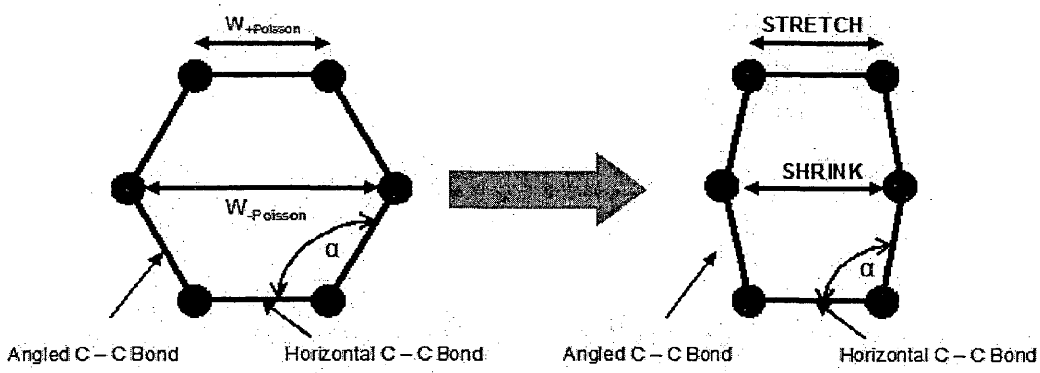

Figure 19. Distorted two-component Poisson effect on polyacene strands.

Simulations conducted under the same conditions as those in Section 3.1.2 yield the transverse elastic responses to axial loading summarized in Table 3.

	POISSON EFFECT @ $W_{+POISSON}$	POISSON EFFECT @ $W_{-POISSON}$
0.5 % Applied Strain	0.322	-0.009
1.0 % Applied Strain	0.332	-0.038
1.5 % Applied Strain	0.322	-0.083
2.0 % Applied Strain	0.321	-0.086

Table 3. Positive (+) and negative (-) Poisson ratios of polyacene strands.

Taking both the positive and negative Poisson effects into account, bulk properties can be recovered using a weighted average technique. Equation 3.4 illustrates the weighted average concept:

$$\nu = \frac{w_{-Poisson}\nu_{-Poisson} + w_{+Poisson}\nu_{+Poisson}}{w_{-Poisson} + w_{+Poisson}} \quad . \tag{3.4}$$

Applying this concept, the following Poisson values were obtained:

APPLIED STRAIN	NET POISSON RATIO
0.5 %	0.209
1.0 %	0.205
1.5 %	0.184
2.0%	0.182

Table 4. Poisson ratio for polyacene strands in uni-axial tension.

The data shows a slight non-uniformity in the Poisson ratios as strain increases. However, each averaged value is well within the range of accepted results for graphite and SWCNTs [6][8][41][42]. Furthermore, independent studies have also found that the Poisson ratio varies with applied strain [43].

The two-component Poisson effect can be explained in terms of the applied boundary conditions and resulting geometries. In modeling the axial applied strain, the overall periodic length is fixed. In other words, the position of the atoms will change minimally in the axial direction. This restriction, induced by the strain, motivates a slight stretch (negative Poisson) in the horizontal bond and a shrink (positive Poisson) at the widest part of the hexagonal structure. In other words, the central atom of the three – body carbon bond will move inward, while the end atoms will move outward, deforming slightly in the direction of a rectangular shape rather than the initial hexagonal structure. This effect can be seen in Figure 19. A single hexagonal component of the Poisson effects of PA is depicted in Figure 20. By examining the two-component Poisson effect, it can be understood that the C – C bond length is more constrictive than the angular dependence of the bond.

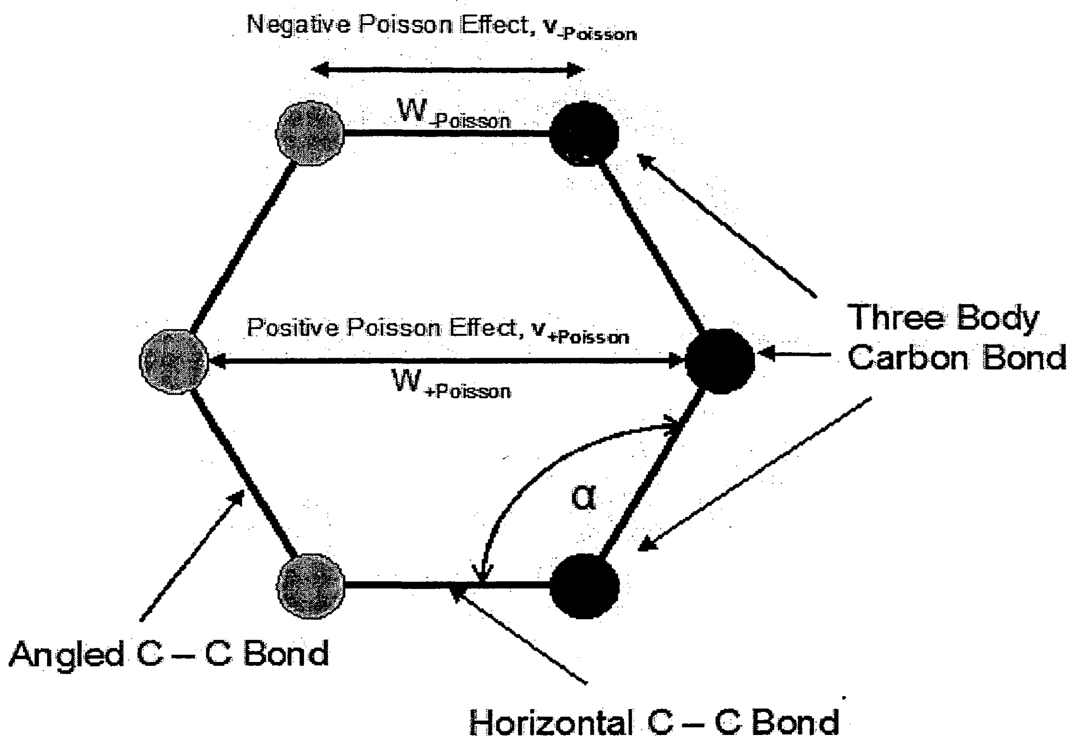

Figure 20. Two-component Poisson effects of polyacene strands.

Using DMOL[3] the same positive and negative partial Poisson effects observed in PA strands were also identified in armchair chirality carbon nanotubes. A summation of these circumferentially allows the transverse strain to be determined. A (5,5) SWCNT was used as a comparison structure to investigate other fullerenes with multi-component Poisson effects. This (5,5) SWCNT was selected because of its computational simplicity and the fact that the armchair chirality is oriented in the same direction axially as the PA strands. The analysis was conducted utilizing a k-point sampling of 1x1x10 (in which 10 k-points are used in the periodic direction). Figure 21 depicts the structures used in analyzing the (5,5) SWCNTs and is identical to Figure 7, used in outlining the uni-axial tension molecular modeling.

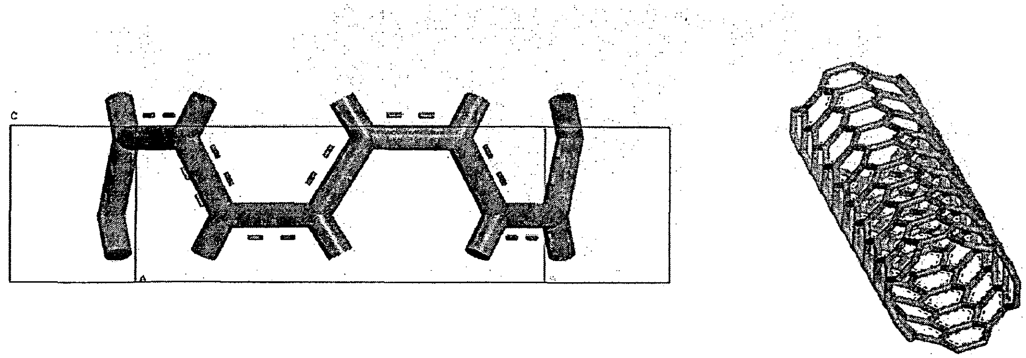

Figure 21. Periodic (5,5) SWCNT unit cell and super cell isometric view.

For a (5,5) SWCNT it can be seen that there is a positive Poisson ratio across $w_{+Poisson}$ of $\nu_{+Poisson} = 0.226$ and a negative Poisson ratio across $w_{-Poisson}$ of $\nu_{-Poisson} = -0.0107$. These two effects yield a weighted average Poisson ratio of $\nu = 0.142$. This value is slightly smaller than that for PA, but is believed to be due to the effects of the high curvature of the (5,5) nanotube; however, similar trends of multi-Poisson effects can be observed. Interesting, the weighted average for a (7,7)—smaller curvature—did not approach the value of for graphene. The weighted average for a (7,7) SWCNT was $\nu = 0.09$. Presently, an explanation for this observation is unclear. Due to the fact that all these systems are comprised of hexagonal carbon structures, intuition suggests that the axial responses (E and ν) will be similar to one another.

Other researchers have reported similar positive/negative trends in nanotubes using molecular dynamics [44]. Additionally, a group of researchers completed an analytical model to relate the chiral angle and size dependent elastic properties to the atomic structure [6]. Their model accomplishes this by incorporating the three-dimensional bond angles and bond lengths for all bonds. These studies offer important descriptions of the elastic properties of small scale carbon nanotubes, but do not discuss the approach of a weighted average to describe the bulk properties.

Again, as seen in the Young's modulus investigation, these effects are seen in Siesta yielding a value $\nu = 0.16939$. Although off slightly from the $DMOL^3$ value of $\nu = 0.142$, both values exhibit the same trends and are within a reasonable degree of uncertainty. However, the two-component Poisson effect is not reproduced when run using CASTEP, a reciprocal space DFT package. The differences are believed to be in applying the reciprocal space approach to non-equilibrated structures (i.e. applied strains).

3.2 Polyacene Bending and Polyacene Rings

Evaluation of the zero-temperature bending modulus of PA strands can be accomplished by applying the mechanics theory developed in Section 2.5.4 to an electronic structure calculation of PA rings of different curvature.

3.2.1 Bending Modulus of Polyacene

As discussed in Section 2.5.4, the pure bending model has been extended to model a ring structure, in which the only energetic effects are due to the curvature of the system. A k-point sampling was not reported here due to the fact that these simulations are non-periodic simulations. As can be seen in the theoretical discussion of Section 2.5, there are geometric parameters that play a role in curvature dependence of the strain energy. These parameters take the form of I, the second moment of area. I is simply based off the cross-sectional geometry of the structure. Since a ring is being investigated, the cross-section of Figure 17 is applied around the circumference of the ring. As a result, the same width and height measurements for this cross-section are used. Figure 22 displays the strain energy as a function of the curvature for PA rings shown in the model of Figure 5.

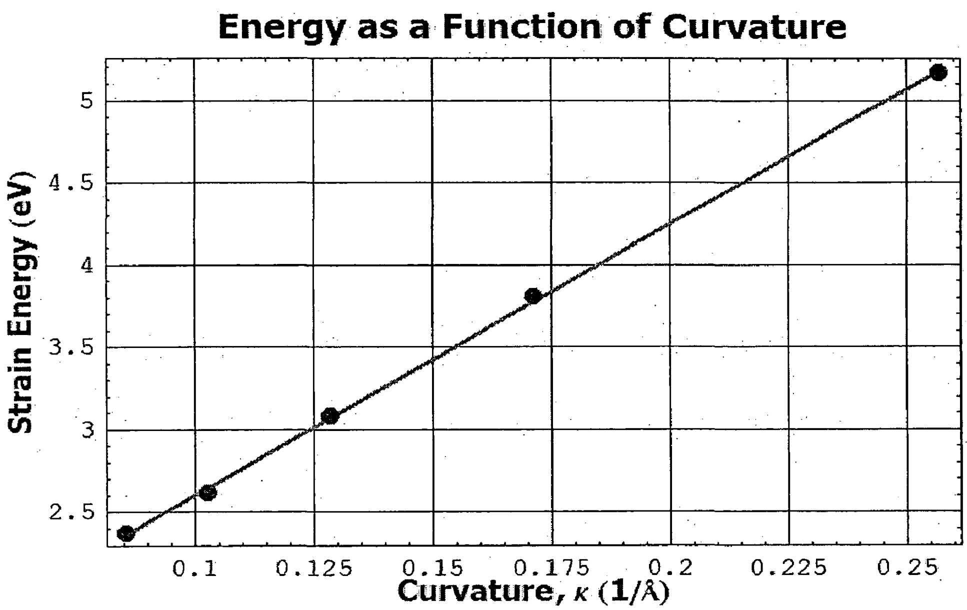

Figure 22. Energy as function of curvature for polyacene rings.

The slope of the above fit, $m = 16.4587$ eV Å, is now set equal to the coefficient of the energy curvature function, πEI from Equation (2.42). From this coefficient, the "bending modulus", $E_{Bending}$, is recovered to be $E_{Bending} \approx 62.9$ GPa for PA strands.

From analysis of the geometries of a PA ring and a SWCNT of zigzag chirality it can be assumed that the energies of both systems will have a similar dependence on curvature. The similarities in geometry stem from both structures having the same bond orientation circumferentially, but with the PA ring being of finite width, while the zigzag nanotube applies periodic boundary conditions along the length of the tube. The geometric similarities can be seen in Figure 23.

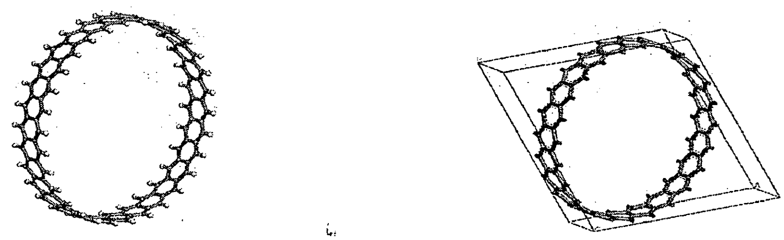

Figure 23. Poly-anthracene ring and (24,0) SWCNT.

A DFT simulation was run using identical parameters as in the case of a PA ring, but utilized a periodic unit cell and a 1x1x6 k-point sampling. Due to the fact that a periodic system is being modeled, a different width is used in calculating the second moment of area. This width is simply, the width of the periodic cell. As a result of using the principle of half a bond length of additional width in determining the cross-sectional size of the PA, it turns out that these two widths are identical. The results describing the strain energy as a function of curvature for a zigzag SWCNT can be seen in Figure 24.

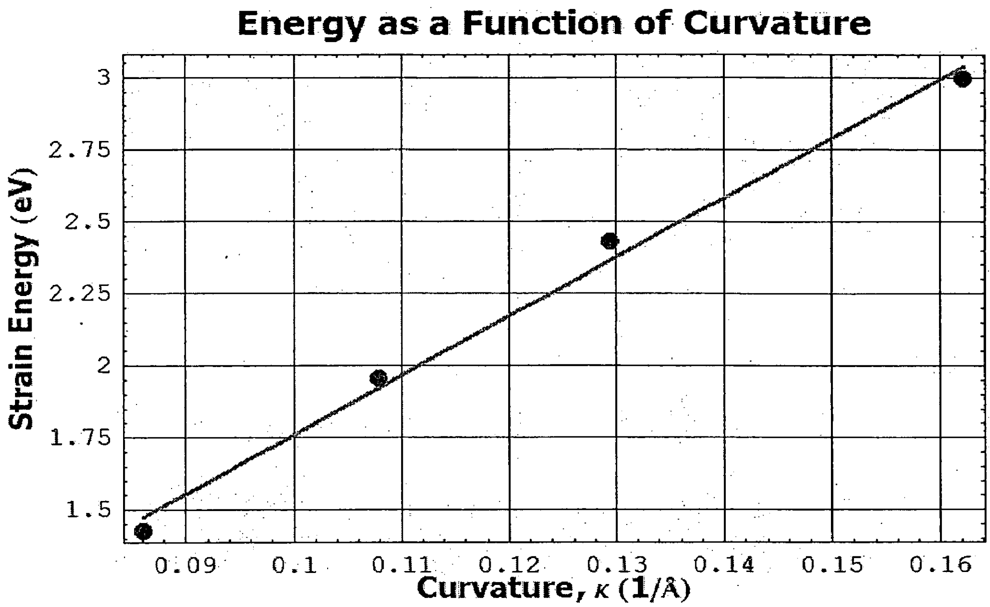

Figure 24. Strain energy as function of curvature for zigzag a SWCNT.

The slope of the above fit, $m = 20.5785$ eV Å, is similarly set equal to the coefficient of the energy curvature function. For the case of zigzag SWCNTs, $E_{Bending} \approx 78.4$ GPa. As expected, the circumferential geometric similarities results in the two bending moduli being similar.

If PA strands were an isotropic material, it could be assumed that the bending modulus parameter would be equal to the Young's modulus. However, as stated previously, we cannot assume a molecule of PA to be isotropic. The reported value is a great deal smaller than Young's modulus for a PA strand or a SWCNT, but can be attributed to the "anisotropy" in the system and localized effect on the π-bonding. This methodology discussed in subsequent sections, provides a foundation for the analysis of the bending modulus of more complicated carbon nanoring systems.

3.2.2 Persistence Length

An interesting quantity in the field of mechanics is that of the persistence length, λ. The persistence length is defined as a length scale beyond which the elastic cost of bending is totally negligible. One of the predominant applications of persistence length in molecular modeling is in the investigation of DNA chains.

Biomolecules like DNA, actin, and proteins are polymers, long chains of similar repeated units.. Moreover, each unit contains some dozens of individual atoms, it is theorized the molecule itself could behave effectively as a continuum object, responding to applied forces as an elastic body, in which an enormous simplification would take place over the complex and unintuitive underlying quantum laws [45].

This concept can be explained simply, by picturing a long, thin elastic material. Imagine a rubber tube, the rubber tube obviously resists bending, but it is much easier to bend the tube into a ring with a large radius than a small one. Correspondingly, the energy cost in forming the ring will become smaller and smaller for rings of larger and larger radii, or in terms of circumference of larger and larger length.. In a molecular system however, these effects are not due to the intiutive length explanation for a macrscopic material, but are due to entropic effecs, thus in lies a temperature dependence. Utilizing a basic understanding of statistical mechanics, we can imagine that there is an exteremely limited number of configurations that will result in the molecule being completely straitght, i.e. have no curvature. On the other hand, there are many more configurations in which the molecule could have a reduced straigth line length. Thus, the straightened molecule, has much less entropy then the un-straightened system. This concept is the basis for a analysis technique known as the worm-like chain model and leads to a dependence on Boltzmann's constant and temperatuere. Persistence length holds the form illustrated in Equation 3.5.

$$\lambda = \frac{EI}{k_B T} \tag{3.5}$$

In which E, I, k_B, and T are defined as the modulus parameter, second moment of inertia, Boltmann's constant, and temperature, respectively.

A study condcuted by Zhang and Shen, has shown there to be a temperature dependence on the elastic properties, Young's and Shear modulus [46]. Although not considered here, it can be asssumed that there will be a corresponding dependence of the bending modulus parameter on temperatuere. However, implementing the bending modulus determined in this investigation, persistence length values are reported in Table 5.

TEMPERATURE	PERSISTENCE LENGTH
30K	810.6 nm
298K	81.6 nm
500K	48.6 nm
1000K	24.3 nm

Table 5. Persistence length as a function of temperature.

In comparison, PA strands are on the same order as the persistence length of DNA. At room temperature, DNA has a persistence length of approximately 50 nm, while PA has a value of 81.6 nm.

3.2.3 Implications of Bending Modulus and Persistence Length of Polyacenes

The importance of investigating the bending modulus and persistence length of PA strands is in applying the mechanical properties to engineering a formation process for both PA rings and carbon nanorings and to aide in the theoretical development of the mechanics of carbon nanorings. The bending modulus of PA strands provides an idea of the stresses that would be needed to bend a PA strand of reasonable length into a PA ring. Additionally, this same idea could be applied to bending, or "rolling", sheets of graphene into SWCNTs or bending a SWCNT into a Type II TCN. The concept of persistence length is of equal importance because it provides an idea of how long the graphene or SWCNT would need to be to bend a specimen into a ring of reasonable curvature. Imagine a beam of steel 1 m long. Not including, fracture effects, it would require a tremendous amount of energy to bend this beam a reasonable amount. However, a steel beam 1 mile long would be much easier to form a ring.

Therefore, even though it has been shown that PAs over a few aromatic rings become highly reactive and are difficult to isolate, does not mean that future researchers will not be able to synthesize PAs of longer and longer lengths. The concepts of the bending modulus and persistence length are crucial parameters in the application of PA structures.

Although the mechanics of PA strands are not directly comparable to the mechanics of carbon nanorings, they can offer valuable insights and a general approach. In both systems, the bending of a molecular structure can be analyzed through the application of a ring structure. Thus, the curvature effects of a carbon nanoring can be used to understand the bending mechanical properties of a SWCNT and likewise the bending properties of a SWCNT can describe the stresses in bending a SWCNT into a

Type II TCN. A similar theoretical approach can be used, except that the fact that the inner diameter of the nanorings has a different curvature than the outer diameter.

3.3 Discussion of Carbon Nanotori

Energy calculations have been conducted in DMol^3 for (3,3) carbon nanorings of the Type II (toroidal polyhexes) TCNs for rings of 120 to 480 atoms. These simulations were conducted under similar conditions as the previous simulations (LDA, spin unrestricted, etc), but applying a medium convergence criterion of 2.0×10^{-5} Ha instead. As in the case of the PA rings there is no k-point sampling here due to the fact that these systems are non-periodic. Additionally, the approach parallels that of the PA ring investigation in which the strain energy is calculated as a function of the curvature.

From the DFT data, a strong empirical $\frac{3}{2}$ power dependence can be seen. It is assumed that this data and the corresponding fit are outside of the harmonic nature of rings of very small curvature—i.e. small deviations from a flat tube. Currently, however, it would be computational impossible to conduct DFT simulations of rings of this radii. Figure 25 illustrates the data and the $\frac{3}{2}$ power fit.

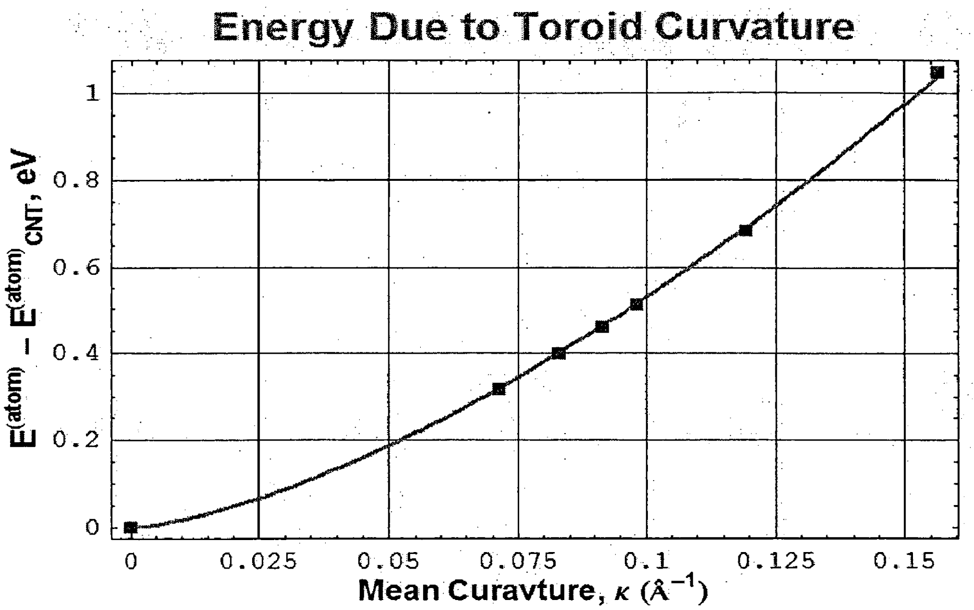

Figure 25. Energy due to toroid curvature for a (3,3) Type II TCN.

It is predicted that there are three contributions to the strain energy of carbon nanorings:

U_1 – Shear contribution to bending

U_2 – Compressive and tensile contributions due to bending

U_3 – Compressive contribution due to toroid thickness due to bending

The third contribution comes from an interesting observation that h, the difference between inner and outer diameters is a function of curvature. Currently however, there is no clear agreement between a theoretical development and the empirical data. The proposed theoretical formulations are not in agreement with the $\frac{3}{2}$ power curvature dependence on the energy. Additional investigations need to be completed to bring the theoretical and experimental values into concurrence.

CHAPTER 4

Conclusion

Richard Feynman said in 1963 that "everything that living things do can be understood in terms of the jiggling and wiggling of atoms" [47]. As the length scales embraced by engineers become smaller and smaller, analysis of the electronic structure of molecular assemblies will become an increasingly important part of the characterization of physical properties. The atomic structures and elastic properties of PA strands and PA rings proves to be very beneficial in application to more complicated graphitic and fullerene like structures (graphene, SWCNT, TCNs). Understanding the complex nature of the responses to uni-axial tension and bending for the simplified systems of PAs has offered valueable insight into the elastic properties of these much more complex systems.

4.1 Summary of Findings

Through a series of electronic structure calculations, this investigation explains the uni-axial tension effects and the curvature dependence of the bending modulus of PA strands. The synthesis of PA strands and PA rings is theoretically possible, but the focus of this investigation is not on a formation process, but on utilizing their mechanical properties as effective tools to study the complexities of TCNs and other complicated curved graphitic structures. It is my contention that this analysis can be used as a stepping stone in determining the curvature effects on the mechanical properties of carbon nanotori.

DFT calculations using $DMOL^3$ give a Young's modulus for a single PA strand of 1.093 TPa. As stated previously, this value is well within the range of reported values for a SWCNT. More importantly, it is extremely close to the accepted value for a single sheet of graphite of 1.06 TPa. Uni-axial tension applied to a single sheet of graphite is very similar to a PA strand supporting the tensile mechanics procedure outlined in this analysis.

From these simulations, an interesting two-component Poisson effect is observed. A negative Poisson effect is seen in the horizontal C – C bonds and a positive one across the widest part of the hexagonal structure. These effects and their geometric properties were illustrated in Figure 19 and 20 in Section 3.1.3. It was shown that using a weighted average of these effects yields a Poisson's ratio comparable to bulk graphite and SWCNTs. The two component Poisson effect suggests that the C – C bond length is more constrictive than the angular dependence of the bond.

Applying a standard pure bending model to a ring, the energetic effects of the curvature can be isolated. The energetic dependence on curvature can result in what is referred to in this investigation as a "bending modulus". PA rings were constructed to separate the curvature effects from other boundary effects, such as finite length effects, to investigate the bending modulus of PA strands. The mechanics theory developed in this study produces the following expression for the strain energy as a function of curvature:

$$U = \pi EI\kappa . \tag{2.42}$$

This expression is a linear relationship for the strain energy as a function of curvature. The linear relationship is a result of the geometric constraint of a ring. A ring has a fixed circumference, in other words a fixed total length, and thus the length of the ring is then a function of curvature. As a result the strain energy does not have the κ^2 relationship of standard continuum beam bending analyses. Data from DFT simulations confirmed this linear dependence on curvature and generated a bending modulus of $E_{Bending} \approx 78.4$ GPa.

Furthermore, the bending modulus was used to make predictions of the persistence length of a PA strand. The persistence length defines the length in which the elastic cost of bending becomes negligible. Although, longer PA strands are known to be extremely reactive, longer and longer PA strands are being synthesized and this parameter has potential applications in determining the length in which PA strands need to be to form a PA ring. More significantly, this concept could be applied to a SWCNT to form a TCN of the form of Type II discussed in Chapter 1. The mechanical properties of PA strands are summarized in Table 6.

	YOUNG'S MODULUS	POISSON'S RATIO	BENDING MODULUS
PA Strands	1.093 TPa	0.18 – 0.21	0.25 TPa

Table 6. Mechanical properties of polyacene strands.

Finally, the PA ring bending theory was used to make a basic prediction for the curvature dependence of TCNs. Simulations similar to those ran for PA rings in $DMOL^3$ were conducted for TCNs. The results show a very strong empirical $\frac{3}{2}$ power dependence. A full description of the theoretical aspects of this dependence are still in development, but are believed to be a result of the multi-component effects of bending seen in TCNs (i.e. curvature effects, compression and tension of inner and outer radii, cross sectional compression).

4.2 Future Research

This thesis contributes to furthering the understanding of the small-scale mechanical effects of carbon nanostructures and provides insights into the study of TCNs, but further work needs to be conducted in both areas. To begin, studies can be conducted for other types of bending, shear, and torsion.

The lack of a unanimous understanding of the small scale bond effects of carbon nanostructures under loading and the discrepencies in the Poisson effects motivates a demand for a concrete description of the mechanics. As was seen in this thesis, a two-component Poisson effect was not observed in the k-space code, CASTEP, and MD is inadequete in describing the effects on individual bond lengths. Further investigation needs to be condcuted to determine the reason for the differences in the Poisson effects in real space and k-space DFT packages.

From the two-component Poisson effect, hypotheses can be made for zigzag and chiral SWCNTs. From the geometric structure of zigzag tubes it can be theorized that the Poisson ratio has only a single positive Poisson component, but there is a two-component effect similar to that discussed for armchair nanotubes on bond stretching when looking at the Young's Modulus. However, the Young's modulus can still be calculated for zigzag tubes without this effect due to the fact that the Young's modulus is calculated from an energetics approach and not from individual bond lengths. From this hypothesis it is believed that there is a linear combination of these effects that can be applied to determine the mechanical properties of nanotubes of all chiralities.

Carbon nanorings offer enormous potential structural, magnetic, and electronic benefits prompting a desire for a complete mechanics description. The theory developed for PA rings can be used as a starting point in analyzing the energetic effects due to the curvature, but it needs to be further developed to understand all the effects occurring in the bending of nanotube-like structures. Additionally, an agreement needs to be reached between the empirical $\frac{3}{2}$ power curvature dependence and the mechanics of the shear contribution due to bending, compressive and tensile contributions within the tube, and compressive contributions due to toroid thickness responses to bending. The complete understanding of SWCNT nanotube bending with respect to nanorings could motivate a carbon nanoring formation from the bending of a SWCNT or similarly for a nanotube of coalesced C_{60} molecules leading to significant applications in structural, magnetic, and electronic devices.

CITED REFERENCES

[1] Markus J. Buehler. "From nano to micro: Introduction to atomistic modeling techniques". Lecture series. CEE, Fall 2005. IAP, Spring (2006).

[2] J. L. Davidson and W. P. Kang. "Carbon nanostructures for device/sensor applications". Interdisciplinary Program in Materials Science – Vanderbilt University. < http://www.ims.vanderbilt.edu/uploads_research/Carbon%20Nanostructures%20for%20Deveice.htm >

[3] O. Castellini, W. deProphetis, L. Nesius, W. Crone, A. Payne. "Carbon nanotubes activity guide". Materials Research Science and Engineering Center, University of Wisconsin – Madison, October (2005).

[4] A. Krishnan, E. Dujardin, T.W. Ebbesen, P.N. Yianilos, and M. M. Treacy. "Young's modulus of single-walled nanotubes". Physical Review B **58** (20_ 14013 (1998).

[5] D. Sanchez-Portal, E. Artacho, J. M. Soler, et al. "Ab initio structural, elastic, and vibrational properties of carbon nanotubes". Physical Review B **59** (19) 12678-12688 (1999).

[6] T. C. Chang, J. Y. Geng, and X. M. Guo. "Chirality and size-dependent elastic properties of single-walled carbon nanotubes". Applied Physics Letters **87** (25) 251929 (2005).

[7] Chen X and Cao GX. "A structural mechanics study of single-walled carbon nanotubes generalized from atomistic simulation". Nanotechnology **17** (4) 1004-1015 (2006).

[8] Kelly, B.T. Physics of Graphite. London: Applied Science Publishers, 1981.

[9] Nan Chen, Mark T. Lusk, Adri C. T. van Duin, and William A. Goddard III.. "Mechanical properties of connected nanorings via molecular dynamics simulation". Physical Review B **72** 085416 (2005).

[10] J. A. Rodríguez-Manzo, F. López-Urías, M. Terrones, and H. Terrones. "Magnetism in corrugated carbon nanotori: The importance of symmetry, defects and negative curvature". Nanoletters **4** (11) 2179-2183 (2004).

[11] H. Terrones, R. Lopez-Urias, E. Munoz-Sandoval, J. Rodriguez-Manzo, A. Zamudio, A. Elias, and M. Terrones. "Magnetism in Fe-based and carbon nanostructures: Theory and applications". Solid State Sciences **8** (3-4) 303-320 (2006).

[12] B. I. Dunlap. "Connecting carbon tubules". Phys. Rev. B **46**, (3) 1933-1936 (1992).

[13] S. Ihara, S. Itoh, and J. Kitakami. "Toroidal forms of graphitic carbon". Physical Review B **47** (19) 12908-12911 (1993).

[14] E. Kurby, R. B. Mallion, and P. Pollak. "Toroidal polyhexes". Journal of the Chemical Society Faraday Transactions **89** 1945-1953 (1993).

[15] V. Meunier, P. Lambin, and A. Luca. "Atomic and electronic structures of large and small carbon tori". Physical Review B **57** (23) 14886-14890 (1998).

[16] M. T. Lusk and N. Hamm. "Toroidal carbon nanotubes with embedded loops of atomic wires". Science (to be submitted) Jan (2007).

[17] H. Terrones, M. Terrones, E. Hernández, N. Grobert, J. C. Charlier, and P. M. Ajayan. "New metallic allotropes of planar and tubular carbon". Physical Review Letters **84** (8) 1716-1719 (2000).

[18] K. Pennicott. "Nanotorus nets giant magnetic moment". Institute of Physics Publishing - PhysicsWeb. May (2002).

< http://physicsweb.org/articles/news/6/5/13/1 >

[19] L. Liu, G. Y. Guo, C. S. Jayanthi, and S. Y. Wu. "Colossal paramagnetic moments in metallic carbon nanotori". Physical Review Letters **88** (21) 217601 (2002).

[20] R. Mondal, B. K. Shah, and D. C. Neckers. "Photogeneration of heptacene in a polymer matrix". Journal of the American Chemical Society **128** (30) 9612-9613 (2006).

[21] S. Kivelson and O. L. Chapman. "". Physical Review B **28** (12) 7236 (1983).

[22] Capelle K. "A bird's-eye view of density-functional theory. arXiv: cond-mat/0211442.

[23] P. Hohenberg and W. Kohn. "Inhomogeneous electron gas", Physical Review Series II **136** B864-B871 (1964).

[24] T. B. Pedersen. "The Hohenberg-Kohn theorems". 20 Oct. (2000).
< http://dcwww.fys.dtu.dk/~bligaard/wwwdirectroy/masterthesis/masterdirectory/project/node10.html >

[25] W. Kohn and L. J. Sham. "Self-consistent equations including exchange and correlation effects". Physical Review **140** A1133-A1138 (1965).

[26] J. Andzelm, E. Wimmer, and D. R. Salahub. "The challenge of d and f electrons". ACS Symposium Series Ser. 394 (1989).

[27] L. Versluis, T. Ziegler. "The determination of molecular structures by density functional theory. The evaluation of analytical energy gradients by numerical integration". Journal of Chemical Physics **88** 322-328 (1988).

[28] N. W. Ashcroft, N. D. Mermin. Solid State Physics. Holt Saunders; Philadelphia, p. 113 (1976).

[29] M. C. Payne, M. P. Teter, D. C. Allan, T. A. Arias, J. D. Joannopoulos. "Iterative minimization techniques for ab initio total-energy calculations: molecular dynamics and conjugate gradients". Reviews of Modern Physics **64** 1045-1097 (1992).

[30] S. Clark. "The pseudopotential approximation". 31 Oct. (1996).
< http://cmt.dur.ac.uk/sjc/thesis/thesis/node20.html >

[31] B Delley. "Hardness conserving semilocal pseudopotentials". Physical Review B **66** 155125 (2002).

[32] J. P. Perdew and Y. Wang. "Accurate and simple analytic representation of the electron-gas correlation energy". Physical Review B **45** 23 (1992).
[33] D. Qian, G. J. Wagner, W. K. Liu, M. Yu, and R. Ruoff. "Mechanics of carbon nanotubes". Applied Mechanics Reviews **55** (6) (2002).

[34] Vosko, S. J.; Wilk, L.; Nusair, M. "Accurate spin-dependent electron liquid correlation energies for local spin density calculations: A critical analysis", Canadian Journal of Physics **58** 1200-1211 (1980).

[35] B. Delley. "An all-electron numerical method for solving the local density functional for polyatomic molecules". Journal of Chemical Physiscs **92** 1 508-517 (1990).

[36] P. Ordejón, E. Artacho, and J. M. Soler. "Self-consistent order-N density-functional calculations for very large systems". Physical Review B **53** 10441 (1996).

[37] José M. Soler, Emilio Artacho, Julian D. Gale, Alberto García, Javier Junquera, Pablo Ordejón, and Daniel Sánchez-Portal. "The SIESTA method for ab initio order-N materials simulation". Journal of Physics: Condensed Matter **14** 2745-2779 (2002).
[38] A. C. T. van Duin, S. Dasgupta, F. Lorant, and W. A. Goddard III. "ReaxFF: A reactive force field for hydrocarbons". Journal of Physical Chemistry A **105** (41) 9396 - 9409 (2001).
[39] Jeroen W. G. Wilder, Liesbeth C. Venema, Andrew G. Rinzler, Richard E. Smalley, Cees Dekker. "Atomic structure and electronic properties of single-walled carbon nanotubes". Nature **391** 6662, 62-64 (1998).
[40] K. M. Liew, X. Q. He, and C. H. Wong. "On the study of elastic and plastic properties of multi-walled carbon nanotubes under axial tension using molecular dynamics simulation". Acta Materialia **52** (9) 2521-2527 (2004).

[41] B. I. Yakobson, C. J. Brabeck, J. Bernholic. "Nanomechanics of carbon tubes: Instabilities beyond linear response". Physical Review Letters **76** (14) 2511-2518 (1995).

[42] A. Pantano, M.C. Boyce, D. M. Parks. "Mechanics of axial compression of single and multi-wall carbon nanotubes". Journal of Engineering Materials and Technology **126** 279-284 (2004).

[43] X. Ni, Y. Wang, Z. Zhang, X. Wang. "Atomic simulation of structure and deformation's influence on mechanical properties of single-walled carbon nanotubes". Chinese Journal of Chemical Physics **19** (4) 197 (2006).

[44] P. Jindal, V.K. Jindal. "Strains in axial and lateral directions in carbon nanotubes". Journal of Computational and Theoretical Nanoscience **3** (1) 148-152 (2006).

[45] P. Nelson. "DNA elasticity". (1999).

< http://www.physics.upenn.edu/~pcn/mcgraw2/mcglatex.html >

[46] C. Zhang and H. Shen. "Temperature-dependent elastic properties of single-walled carbon nanotubes: Prediction from molecular dynamics simulation". Applied Phyiscs Letters **89** 081904 (2006).

[47] M. P. Allen, D. J. Tildesley. Computer Simulation of Liquids. Oxford University Press. ISBN 0-19-855645-4. (1989).